Universidad del Norte

Master Thesis

Analysis of Potential and Efficiency of Electric Generation Using Thermoelectric Effect

Author:
Daniela Charris Stand

Advisor:
Mauricio Pardo González, PhD

A thesis submitted in fulfillment of the requirements
for the degree of Master of Science on Electronics Engineering

in the

Robotics and Intelligent Systems Research Group
Electrical and Electronics Engineering Department
Universidad del Norte

July 2019

UNIVERSIDAD DEL NORTE

Abstract

Electrical and Electronics Engineering Department
Robotics and Intelligent Systems Research Group

Master of Science on Electronics Engineering

Analysis of Potential and Efficiency of Electric Generation Using Thermoelectric Effect

by Daniela Charris Stand

This research identifies the electrical potential associated with Thermoelectric Generators (TEG) under the incidence of solar rays and performs efficiency comparison using this type of devices and those photovoltaic. TEG characterization and modeling is presented to favor the estimation of the electrical potential, defined as power density (W/m^2). The proper operation of thermal harvesting lays in maintaining a temperature difference of at least 26.31K between the TEG sides. With this requirement fulfilled, power conversion efficiencies of about 26.43% are obtained, higher than that of high-quality solar panels and without efficiency reductions associated with heating and soiling, while keeping the same superficial area of only $16cm^2$. An estimate of at least 407.3mW corresponding to 2.44Wh of available energy is found considering specific operation hours determined statistically for a given geographic location. Thus, given such performance metric, a complete power unit is devised complementing the thermoelectric energy harvesting with a Li-Po battery to guarantee in that way a continuous operation. The total energy available from the prototype allows maintaining a battery discharge percentage of 38.05% considering the energy budget of a low-power remote sensor.

Acknowledgements

"No one who achieves success does so without acknowledging the help of others. The wise and confident acknowledge this help with gratitude"

Alfred North Whitehead

First and above all, I praise God for giving me the strength, knowledge, ability and opportunity to undertake this research study. Without his blessing, this achievement would not have been possible. I would like to offer my sincere thanks to all the people who gave me assistance and guidance during this time.

My sincere gratitude goes to my advisor, Dr. Mauricio Pardo, for the continuous support during this study, for his patience, motivation, and immense knowledge. His guidance helped me in all the time of research and writing of this thesis. I could not have imagined having a better advisor and mentor.

Besides my advisor, I would like to thank Prof. Diego Gómez for his insightful comments and encouragement. Also, I thank Dr. Mauricio Carmona and Anggie Rincón, from the Mechanical Engineering Department, for their support in the study of phase change materials. I gratefully acknowledge the funding received through *Francisco José de Caldas Fund*, the National Fund for Financing Science, Technology and Innovation in Colombia.

I would like to thank my labmates and friends José Manjarrés, Catherine Díaz and Mauro Jiménez, for the stimulating discussions, for company at the sleepless nights at lab -or Cathe's house- we were working, and for all the fun we have had in the last two years. I also thank Jorge Martínez for joining me during the weekends that I stayed until night working.

Last but not the least, I like to thank my family: my mother and to my aunt (a.k.a. mom) and cousin (a.k.a. sister) for supporting me spiritually throughout writing this thesis and in my life in general.

To all of them my acknowledgments and gratitude.

Contents

Abstract i

Acknowledgements ii

Contents iii

List of Figures v

List of Tables vii

List of Abbreviations viii

1 Introduction 1

2 Research Problem 3
2.1 Background . . . 3
2.2 Problem Statement . . . 5
2.3 Justification Statement . . . 6
2.3.1 Scientific-Technological Impact . . . 7
2.3.2 Impact on Productivity and Competitiveness . . . 7
2.3.3 Impact on the Environment and Society . . . 8

3 Research Objectives 9
3.1 Aim . . . 9
3.2 Objectives . . . 9
3.3 Delimitations . . . 9
3.3.1 Assumptions . . . 9
3.3.2 Limitations . . . 10

4 Theoretical Framework 11
4.1 Energy Harvesting . . . 11
4.2 Thermoelectric Generator . . . 13
4.3 Phase Change Materials . . . 16
4.4 Solar Panel . . . 17
4.5 Power Management Unit . . . 19
4.5.1 Maximum Power Point Tracking . . . 22

4.6 Storage Units . . . 23
4.6.1 Batteries . . . 23
4.6.2 Supercapacitors . . . 25

5 Related Work 26

6 Proposed Approach 30
6.1 Characterization of Energy Transducers . . . 30
6.1.1 Thermoelectric Module TEC-12706 . . . 30
6.1.2 Solar Module 2V-50mA . . . 33
6.2 Establishment of TEG Operating Conditions . . . 36
6.2.1 Phase Change Material Preparation . . . 38
6.2.2 Temperature Gradient Conditions . . . 40
6.3 TEG Model Validation . . . 42
6.3.1 Validation of Maximum Power Point . . . 43
6.3.2 Validation of Voltage at Maximum Power Point . . . 43
6.4 Prototype Description . . . 44
6.4.1 Power Management Unit . . . 44
6.4.2 Load: Case Study of EFM32 microcontroller . . . 47
6.4.3 Energy Storage . . . 48
6.5 Arrays . . . 49
6.5.1 2-TEG array . . . 49
6.5.2 3-TEG array . . . 50
6.5.3 4-TEG array . . . 51

7 Experiments and Results 54
7.1 Comparison Between Phase Change Material and Metal Heat Sink . . . 54
7.2 Comparison Thermoelectric Generator and Solar Panel . . . 56
7.3 Thermoelectric Energy Harvesting Performance Tests . . . 57
7.3.1 Performance of the DC-DC Converter . . . 57
7.3.2 Performance of the TEH prototype . . . 58
7.4 Efficiency of Arrays with DC-DC converter . . . 61

8 Conclusions and Future Work 63

A Certificate of Attendance 65

B Student Travel Grant 66

Bibliography 67

List of Figures

2.1 Solar energy density in the Caribbean region . . . 3
2.2 Monthly average PSH in Barranquilla, Colombia . . . 4

4.1 Electric model of transducers . . . 12
4.2 EH general block diagram . . . 13
4.3 TEG internal components . . . 14
4.4 First order transducer equivalent model of a TEG . . . 15
4.5 TEG *V-I* and *P-I* characteristic curves . . . 16
4.6 PCM *T-Q* characteristic curve . . . 17
4.7 SP electrical model . . . 18
4.8 Theoretical *I-V* curves for SPs . . . 19
4.9 A basic linear regulator . . . 20
4.10 DC-DC converters . . . 21
4.11 Battery internal components and electrical model . . . 23
4.12 Structure of a supercapacitor . . . 25

6.1 Experiment configuration from TEG parameters estimation . . . 31
6.2 TEG characteristic curves constructed with validated parameters . . . 32
6.3 Curves constructed for temperature gradient selection . . . 33
6.4 Selected SP for comparison . . . 34
6.5 Approximation of the *I-V* characteristic curve . . . 35
6.6 Approximated I-V characteristic curve . . . 35
6.7 Metal plate for TEG hot side . . . 36
6.8 Hot plate temperature during the day . . . 37
6.9 PCM encapsulating preparation . . . 39
6.10 Experimental setup for PCM . . . 39
6.11 Testbench for PCM . . . 40
6.12 Operating conditions for TEG . . . 41
6.13 TEG curves for the selected operating conditions . . . 42
6.14 Prototype block diagram . . . 44
6.15 LTC3105 DC-DC converter model . . . 45
6.16 LTC3105 DC-DC converter transient response from LTSpice . . . 46
6.17 2-TEG array . . . 49
6.18 3-TEG array . . . 50
6.19 4-TEG array . . . 52

7.1 Testbench for heatsink and PCM . . . 54
7.2 Measurements of Δ_T during the day . . . 55

7.3 Dimension comparison between TEG and PV panel 56
7.4 Measurements of output voltage and power of DC-DC converter 58
7.5 Measurements of power delivered by the TEG during selected ranges . . . 59
7.6 Average no-sun days per month 61

A.1 Certificate of attendance and presentation at international conference . . 65

B.1 Certificate of student travel grant 66

List of Tables

2.1 Hourly range with similar radiation 4
2.2 Power densities for energy harvesting 6

4.1 Comparison between EH sources 13
4.2 Comparison between secondary batteries and supercapacitor 25

6.1 Comparison between polycristalline SPs 33
6.2 SP main parameters 34
6.3 Results of the approximation of SP model 36
6.4 Confidence intervals for *mean* hot temperature 37
6.5 TEG main parameters 38
6.6 PCM main properties 38
6.7 Confidence intervals for mean temperature gradient 41
6.8 TEG expected power and energy 42
6.9 Theoretical MPP conditions 43
6.10 Comparison between different DC-DC converters 45
6.11 Energy budget for TEH 47
6.12 2-TEG theoretical results 49
6.13 2-TEG simulated results 50
6.14 3-TEG theoretical results 51
6.15 3-TEG simulated results 51
6.16 4-TEG theoretical results 52
6.17 4-TEG array results 53

7.1 TEG efficiency with optimum R_L. 57
7.2 Percentiles for solar radiation. 59
7.3 TEG harvested energy 61
7.4 Overall efficiency of arrays 62

List of Abbreviations

TEG	Thermoelectric Generator
TEH	Thermoelectric Energy Harvesting
IoT	Internet of Things
EH	Energy Harvesting
SP	Solar Panel
STC	Standard Tests Conditions
PCM	Phase Change Material
PSH	Peak Sun Hours
WSN	Wireless Sensor Network
PZT	Piezoelectric Transducer
OCV	Open Circuit Voltage
MPP	Maximum Power Point
MPPT	Maximum Power Point Tracking
P&O	Perturb and Observe
IC	Incremental Conductance
PC	Parasitic Capacitance
DoD	Depth of Discharge
RTEG	Road Thermoelectric Generator

Dedicated to my family...

Chapter 1

Introduction

Keywords: Energy harvesting, thermoelectricity, thermoelectric generator, solar panel, efficiency, radiation, phase change material.

Smart cities initiatives emerge from the effort of the Internet of Things (IoT) to tackle the raising problems of modern cities. Exploiting innovating technologies, they pretend to improve the quality life of citizens by monitoring the environment and interacting with it [1]. With the principle of interconnected people and objects, IoT applications collect information from autonomous devices and permits the communication between machines. As a result, information about education, energy, healthcare, public transportation, employment, among others, is available on demand in a centralized system like the Internet. To guarantee a continuous operation; challenges as low cost, low power consumption, low range of transmission and easy deployment appear for the successful implementation of IoT solutions [2].

The performance of IoT is based not only on the design and installation of sensors and devices that send the information, or the communication platform, but also on the continuous operation of the associated devices [3]. Designing low power microcontrollers represents an improvement for minimizing the energy consumption. However, available battery technologies have low energy density and operation lifetime continues to be limited [4].

Energy Harvesting (EH) techniques are considered as a solution for complementary power sources. They collect a very small amount of power for low-energy electronics from the environment. Thus, outdoor radiant energy coming from the sun can be used to produce electricity through the photovoltaic effect using Solar Panels (SP) [5]. For outdoor devices, SP can provide the required operation power but only during proper radiation conditions. In any case, the solar resource is usually unpredictable and it needs

to be combined with energy storage units. Also, SP efficiency is affected by dirt and temperature causing an increase in initial deployment and higher maintenance costs. It has been found in the literature and tests that the efficiency does not exceed 20% of the potential [6].

An alternative that is not affected by dirt; and, unlike the solar panel, takes advantage of the sun in terms of heating is the Thermoelectric Energy Harvesting (TEH). A thermoelectric generator is used as transducer of the temperature difference across it [7]. Many approaches have been proposed to guarantee a continuous operation for outdoor devices using only TEH [8]. According with the state-of-the-art, temperature differences do not surpass 15K using the sun as energy source [9]. This results in low power and low thermal efficiency for TEG. Hybrid systems pretend to combine photovoltaic and solar thermoelectric effect to improve the output power. However, this method does not succeed because the concentration scheme produces an undesired increase on the solar panel temperature and does not tackle the dirt associated efficiency reduction. As a result, the efficiency of a hybrid system is still limited by the solar panel operation.

This thesis proposes an approach to exploit the large amount of solar resource available in the Colombian Caribbean region, where the study of TEH takes place. The solar incident radiation is converted into heat by means of a metal surface that acts as concentration element to obtain higher temperature differences. One of the main challenges when using a TEG is to maintain the temperature on the plates. Thermal management relies on the combination of materials and heat transfer techniques to stabilize the component temperature. Cooling mechanism are used in the TEG cold plate to maintain the temperature in desired values. Among the considered methods, fans, heat sinks and materials such as water stand out [10]. Taking into account that is desired to maintain the temperature of the cold plate as constant as possible, this work analyzes the posibility of using a Phase Change Material (PCM) as a thermal stabilizer.

The reminder of this thesis is organized as follows. First, the research problem, justification and expected impacts are presented in Chapter 2. The research objectives are proposed in Chapter 3. Chapter 4 presents theoretical concepts, while Chapter 5 provides related work in thermal energy harvesting. After that, Chapter 6 illustrates the proposed approach of thermoelectric energy harvesting scheme, and Chapter 7 shows quantitative and qualitative results of the experiments, including discussions that emerge from this. Finally, the thesis is concluded in Chapter 8.

Chapter 2

Research Problem

2.1 Background

According to reports delivered by government and worldwide agencies, the Colombian Caribbean region presents a high availability of solar resources. The atlas of solar radiation, ultraviolet and ozone of Colombia reports that solar energy density ranges between 4.5kWh/m^2 and 6kWh/m^2, which are considered high values compared to other regions of the country (see Figure 2.1) [11].

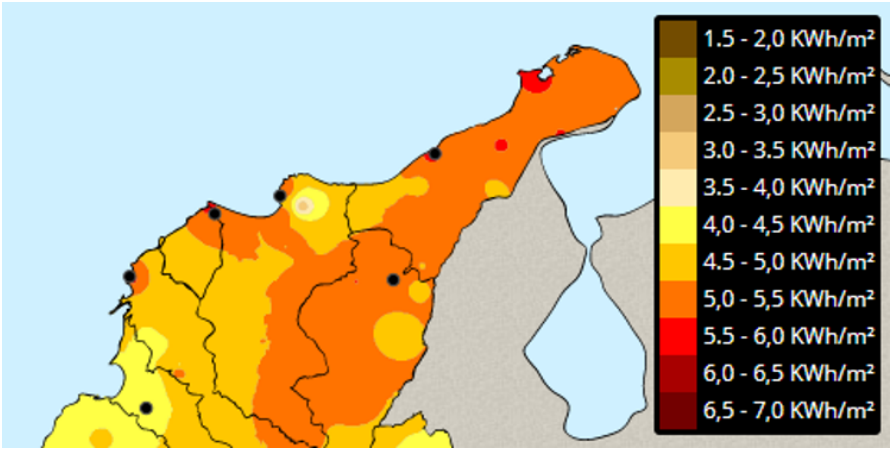

Figure 2.1: Solar energy density in the Caribbean region (taken from [11]).

Peak Sun Hours (PSH) represent the amount of available solar energy in an area during a typical day [12]. One PSH is an hour during which the intensity of sunlight is 1kW/m^2. The Surface Meteorology and Solar Energy from the National Aeronautics and Space Administration (NASA) reports that peak sun hours can vary between 5.56 and 6.89 in Barranquilla, Colombia [13]. Figure 2.2 present the monthly average PSH with the data presented by [13].

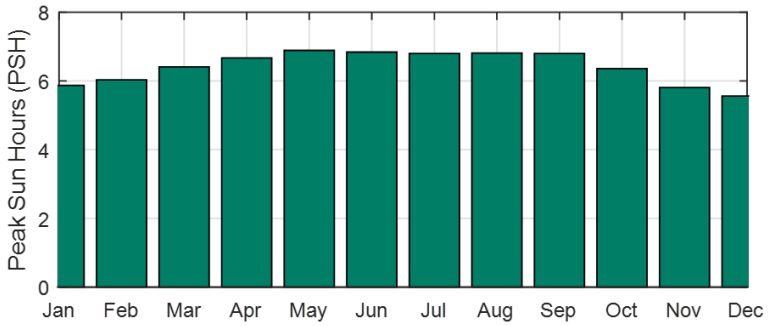

Figure 2.2: Monthly average PSH in Barranquilla, Colombia (data from [13]).

The Electrical and Electronics Engineering Department of Universidad del Norte has developed several projects associated to study the large amount of solar resource in the region. Part of the work developed in this line include the Strategic Area of Energy, the Photovoltaic Solar Energy Laboratory, the Renewable Energy Module and UniGrid, the micro-grid installed in one of the laboratories in Universidad del Norte. Also, courses and diplomas have been opened that allow an approach to solar energy, such as *Special Topics: Renewable Energy* and *Diploma in Generation Projects with Non-Conventional Energies and Smart Grids*.

A particular design of experiments of the Strategic Area of Energy is considered to define solar radiation categories during the day by recognizing their statistical characteristics. To identify these categories, historic data between years 2009 and 2015 are analyzed. Then, the categories are selected based on the Fisher's Least Significant Difference method (LSD). This method starts with the assumption that all groups under study are equal and is chosen because it permits to reject that null hypothesis [14]. The results of applying LSD show that the day is divided in hour ranges following if a statistical difference exists among those. The method is based on the F-ratio to determine if the averages of two similar categories are statistically equal; or, on the other hand, they are not. As observed in Table 2.1, an average day in the city of Barranquilla can be divided into six ranges with Ranges V and VI displaying the highest average radiation estimates.

Table 2.1: Hourly range with similar radiation.

Category	**Hour Ranges**	**Average Solar Radiation [W/m^2]**
I	00:00 - 05:59 / 18:00 - 23:59	0.00
II	06:00 - 06:59 / 17:00 - 17:59	64.65
III	07:00 - 07:59 / 16:00 - 16:59	216.73
IV	08:00 - 08:59 / 15:00 - 15:59	471.61
V	**09:00 - 09:59 / 14:00 - 14:59**	**692.58**
VI	**10:00 - 11:59 / 12:00 - 13:59**	**839.71**

The Journal of Progress in Photovoltaics: Research and Applications reports the advances on photovoltaic research and the improvement on cells efficiency each six months. According to Version 53 (December 2018), a record of 29.1% was measured for a $1cm^2$ single cell, but the overall efficiency decreases when the cells are connected in series or parallel [6]. With the information gathered in the projects, courses and in the literature, it has been demonstrated that electrical energy systems powered by photovoltaic effect have an overall efficiency no greater than 20% [15–19].

The limited efficiency of the panels is induced by the materials used to produce them and the operating conditions. However, it is necessary to improve the energy produced from sun radiation to substantially increase the behavior of the panel. Commonly used methods include: tracking of solar rays, concentration of sunlight and self-cleaning. With the tracking system, the rays are maintained perpendicular to the surface of the solar panel, while constant cleaning avoids the soiling effect produced by the dust particles [20]. In [21], an active cooling mechanism is experimentally evaluated. It is installed under the solar panel and activated or deactivated according to the temperature measured with a termocouple. The use of a compressor decreases the solar panel temperature and the output power range becomes 24.6% higher than the output power of a system without cooling. In [22], a robot which cleans a solar panel is designed. The robot consists of a cleaning head that moves through the surface. From the results, the efficiency increases by 31.23% just after cleaning. On the other hand, using concentrators to direct solar rays improves efficiency in power generation for photovoltaic technologies [23]. Such is the case of [24], where mirrors and an active cooling mechanism are used increasing efficiency to 32% with the concentration scheme and to 52% with concentration plus cooling. However, in [21],[22], [23] and [24]; the power consumption of the used strategies is not evaluated.

Recently, the possibility of using thermal energy harvesting with thermoelectric materials has been explored [25]. Taking advantage of the heating produced by the incidence of solar rays on the Earth's surface, a TEG allows to obtain usable electrical energy by means of the Seebeck effect. With low cost TEGs it is possible to harvest energy by maintaining a temperature difference between their plates [26].

2.2 Problem Statement

The most common power sources for energetically autonomous devices are batteries and energy harvesters [27]. From a Wireless Sensor Network (WSN) point-of-view, the choice of the powering unit is not a trivial issue since a network can contain hundreds (or thousands) of sensors. The power supply can be a primary battery which are simple

to implement but the lifetime of the sensor is limited by the battery capacity [28]. Even though the lifetime can be measured up to years, the process of changing batteries could cumbersome if the sensors are not easily accessible. On the other hand, secondary batteries can be used, but the repetitive process of charging needs to be as automatic as possible and the unit in command requires power management circuitry that maximizes the battery lifetime [29].

Energy harvesters can transform energy constantly from environmental sources to power up remote sensors for longer time periods. Table 2.2 present energy densities for most common environmental sources.

Table 2.2: Power densities for energy harvesting [30–32].

Energy Source	**Energy Density** $[\mu W/m^2]$	**Transducion process**
Solar	150 (Cloudy)	Photovoltaic
	15000 (Sunny)	Photovoltaic
	6 (Indoors)	Photovoltaic
Temperature gradie1nt	40-100	Thermoelectric
Vibration	330	Piezoelectric
	0.021-3.8	Electrostatic
	184-306	Electromagnetic

Although the solar energy density is higher compared to ambient temperature gradient, for example; the selection of the proper transducer can make a significant difference in the available electric power. From an outdoor point-of-view, solar energy can be harvested by solar panels that produce a DC output. In this case, the resulting available energy is affected not only by factors such as position, weather conditions, time and day of the year, but also in soiling effect due to particulate material and cell temperature that reduces the SP efficiency [33, 34]. The SP efficiency is defined as the percentage of the solar energy falling on its surface that is converted into electrical energy. Typically, the SP efficiency is considerably low. Also, solar energy is not only transformed into electrical energy through the photovoltaic effect, but also produces thermal energy manifested in the heating of the SPs, which reduces their efficiency [35].

2.3 Justification Statement

To overcome the challenge of automating the charging process for secondary batteries and, in the process, count with energy available for sensor operation, energy harvesting can be employed as alternative power supply from external sources [36]. The selection

of the ambient source depends on the energy density at the location and on the power required to maintain load operation. Currently, for IoT applications, the required power density can be defined as low, which opens the possibility of using a wide range of sources for energy harvesting. Some of those sources include solar radiation, vibrations, and temperature gradients, among others [37].

Such low efficiency permits to explore alternative ways to harvest the solar resource by different means with higher efficiency. Hence, since variations in temperature produce electricity using thermoelectric or pyroelectric transducers, TEH can also be proposed as harvesting scheme using a TEG [38]. In this case, a TEG converts temperature differences across its plates into electricity [39]. The main challenge comes with devising an strategy to increase or just maintain the temperature difference between the TEG plates/sides to obtain enough energy densities to power an IoT sensor properly [39]. Once the temperature difference is addressed with a dissipative material, the soiling effect becomes irrelevant for the TEG option.

In any case, adequate power management becomes crucial for proper sensor operation. Thus, as the total equivalent load changes, the supply system must be capable of providing sufficient amount of power. Therefore, many DC power supply designs require a regulated output for its operation. Finally, as SP and TEG output power changes with radiation and temperature, performing a search of the maximum power point is also mandatory, so that total supply efficiency is further maximized [40].

2.3.1 Scientific-Technological Impact

This research seeks to estimate the electric energy available by thermoelectric effect under the concentrated incidence of solar rays. The aim is to propose a energy harvesting scheme that permits to power outdoors sensors and devices up with higher efficiencies than solar panels. This contributes to tackle the energy challenges of current communication technologies.

2.3.2 Impact on Productivity and Competitiveness

With this research it will be possible to determine the energy density available and the efficiency of thermoelectric energy harvesting with sun as energy source. This allows the establishment of generation schemes with non-conventional sources that still use solar radiation as their main source and take advantage of this highly available resource in the Caribbean region.

2.3.3 Impact on the Environment and Society

The implementation of low-power generation schemes with renewable energies, such as solar radiation, contributes to the reduction of pollution produced by other solutions. Also, using energy harvesting techniques to power up outdoors sensors and devices decreases the amount of electronic waste produced.

Chapter 3

Research Objectives

3.1 Aim

This thesis aims to develop a comparative analysis of the generation potential and efficiency of a thermoelectric energy harvesting scheme and photovoltaic solar cells.

3.2 Objectives

- To estimate the density of energy available from generation devices by thermoelectric effect from solar energy concentration.
- To develop a comparative analysis of energy efficiency given a unit area of thermoelectric generators with that exhibited by photovoltaic panels.
- To establish an area-efficiency relationship for a thermoelectric energy harvesting scheme composed of an array of thermoelectric generators.

3.3 Delimitations

3.3.1 Assumptions

- The number of low cost thermoelectric generators will be greater than or equal to 2.
- Based on the power generated, the performance of the scheme will be compared with that of a solar panel with electricity production and a similar area.

- The generators will be placed on a metal plate, which will be exposed to the sun.
- It will be taken W/m^2 as energy density unit, in order to make the comparison with photovoltaic solar energy.

3.3.2 Limitations

- Work will be done on basic electrical models based on Thevenin equivalents that reproduce the behavior of thermoelectric modules.
- It is not planned to develop life cycle performance tests of the devices.
- It is not planned to develop tests for disturbances such as dirt, but both systems (photovoltaic and thermoelectric) will be analyzed under optimal environmental conditions.

Chapter 4

Theoretical Framework

This chapter presents the theoretical concepts necessary for the development of this thesis. It includes principles of energy harvesting with its different components, the operation of thermoelectric generators and the solar panels, techniques to obtain the maximum power from non-linear sources, and phase change materials as dissipative elements.

4.1 Energy Harvesting

Energy harvesting is the process by which energy is converted to electricity from environmental sources. Ambient energy sources are present and available in terms of heat, movement or radiation. Given that, EH main purpose consists of capturing ambient energy, transforming into electrical energy and powering wireless sensor nodes, wearable devices and many more consumer electronics. Harvested energy can be categorized into five types: radiant, mechanical, thermal, magnetic and biochemical [36].

Electromagnetic waves emit **radiant energy** that can be categorized in solar and radiofrequency based on the electromagnetic spectrum. Solar energy covers from infrared to ultraviolet light. Outdoors, the available power comes from the sun and depends on factors such as position, weather conditions, time and day of the year. But indoor "solar" energy comes from artificial illumination and windows. In general, solar energy is harvested using photovoltaic cells that produce a DC output [41]. Section 4.4 explains in more detailed the conversion principle and modeling of solar panels. On the other side, radiofrequency energy is emitted by broadcasting stations and cellular antennas in the nanowatt range. The corresponding transducer is a radiofrequency antenna modeled as an AC voltage source, V_{OC}, in series with an output impedance ,Z_S, as shown in Figure 4.1 *(a)*).

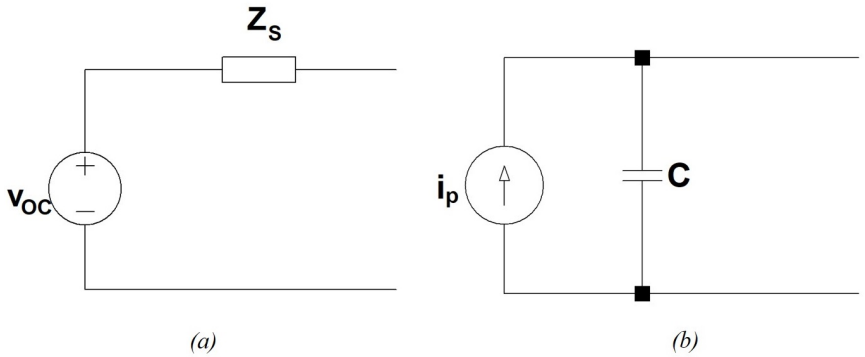

Figure 4.1: Electric model of transducers (adapted from [36]). *(a)* Antenna *(b)* Piezoelectric material

In EH, kinetic energy from vibrations, human activity, pressure variations and gas flow are used as **mechanical energy** source [36, 42]. This type of energy can be transformed by one of three following conversion principles: electrostatic [43], piezoelectric [44] and electromagnetic [45]. Variable capacitors are used in electrostatic EH by changing one of the plates with mechanical force. The piezoelectric effect is explained by the response of mechanical stress in a material. Also, electromagnetic induction is fulfilled using a permanent magnet as magnetic flux source generating a voltage in a conductor [46]. Regardless of the conversion principle, the output power is AC and must be rectified.

Variations in temperature produce electricity using **thermal energy** as source. In the thermoelectric effect, temperature differences in a semiconductor material can cause an electrical energy through the Seebeck effect. Thermoelectric operating principle is explained in Section 4.2. A voltage produced by variations in temperature over time evidence pyroelectric effect. Piezoeletric Transducers (PZT) are considered pyroelectric converters modeled as an AC current source, i_p, in parallel with a capacitor (See Figure 4.1 *(b)*).

On the other hand, current conductors in lines of transmission, magnets or electric rotating machine produce an AC **magnetic energy** by Wiegand effect or induction coils. Wiegand effect consists of generating electricity in a coil by changes in an external magnetic field [47]. The coil is modeled as an AC voltage source.

Chemical-to-electrical conversion is used in batteries to provide portable electricity. In **biochemical energy** the fuel is biological material and it is transformed into DC electricity in an electrochemical reaction [48].

The selection of the ambient energy source depends on the energy density at the location and on the power required to maintain load operation. Table 4.1 compares each energy source's conversion principles, transducers and type of output power.

Table 4.1: Comparison between EH sources.

Type of energy	Transducer	Conversion principle	Output
Radiant	Solar panel	Photovoltaic	DC
	Antenna	Polarization	AC
Mechanical	Variable capacitor	Electrostatic	AC
	Piezoelectric material	Piezoelectric	AC
	Coil	Electromagnetic induction	AC
Thermal	Thermoelectric material	Thermoelectric	DC
	Pyroelectric material	Pyroelectric	AC
Magnetic	Coil	Electromagnetic induction	AC
Biochemical	Biological material	Electrochemical reactions	DC

Regardless of the energy source, any EH system can be expressed with the block diagram of Figure 4.2. The transducer is responsible for taking energy from the environment and converting it into electricity. Thermoelectric generators and solar panels are presented as transducers for solar energy in the Sections 4.2 and 4.4. Due to the stochastic nature of the energy source, any EH system requires a power management unit that allows to operate at the maximum power points, to deliver the power required to the load and also to store the remaining energy for the times where the source is not present. Section 4.5 explains the power management unit and Section 4.6 presents storage units for EH.

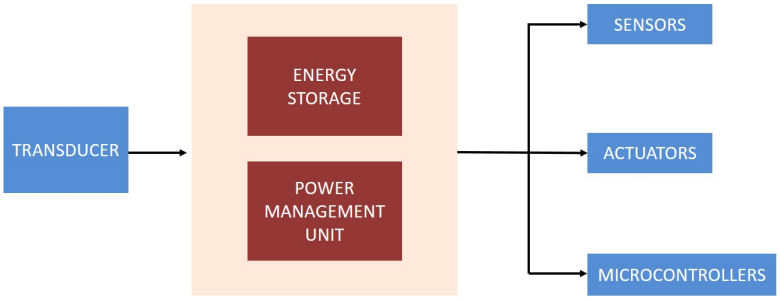

Figure 4.2: EH general block diagram (adapted from [49]).

4.2 Thermoelectric Generator

A thermoelectric generator is a transducer that converts the temperature differences on its sides/plates directly into electrical energy. A TEG is internally composed of a semiconductor material that is doped, producing P-type and N-type legs. These materials are electrically connected in series and thermally connected in parallel, as shown in Figure 4.3.

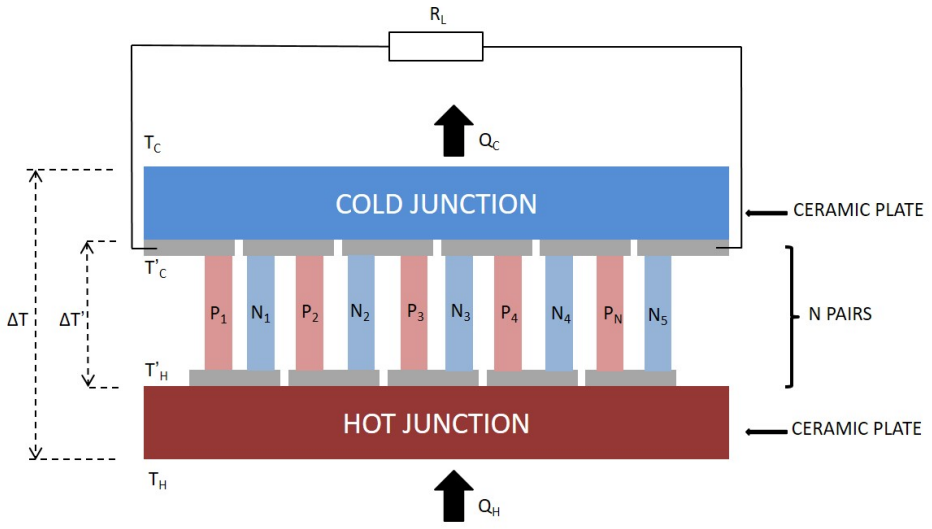

Figure 4.3: TEG internal components (adapted from [50]).

Under the presence of a temperature difference, charge carriers migrate from the hot side to the cold side producing electricity, this is known as Seebeck effect [51]. Using constant parameters such as thermal resistance of the material, contact resistance between its terminals and the Seebeck coefficient, the amount of heat in the hot and cold plates (Q_H and Q_C) can be expressed as

$$Q_H = \frac{T_H - T_C}{\theta_m} + \alpha T_H I - \frac{1}{2} R_E I^2 \alpha, \tag{4.1}$$

$$Q_C = \frac{T_H - T_C}{\theta_m} + \alpha T_C I + \frac{1}{2} R_E I^2 \alpha, \tag{4.2}$$

where T_H and T_C are the temperatures in the hot and cold plates; R_E and θ_m are the electrical and thermal resistances of the N pairs, and α the Seebeck coefficient [52].

After analyzing the thermal behavior of the TEG, it is necessary to analyze its electrical behavior. To obtain an equivalent circuit model, the first step is to define circuit elements for the thermal variables. For that task, it is required to find lumped elements that help to describe the fundamental physics associated. For the TEG, it is enough by defining single-port elements. Thus, in the thermal domain, the effort or across variable (voltage) can be associated with temperature difference, the flow or through variable (current) can be related with a heat current, and the dissipative element (resistors) are electrical and thermal resistors [53]. Therefore, in its simplest form, a TEG can be modeled using the electrical equivalent shown in Figure 4.4. It consists of a voltage source (V_{OC}) in series with a resistance (R_E).

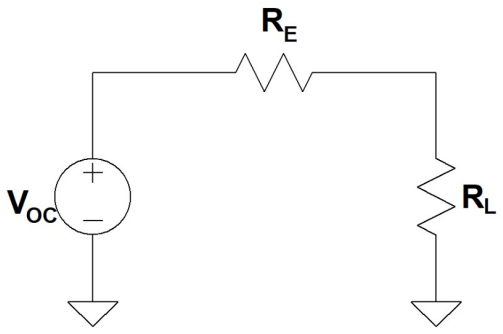

Figure 4.4: First order transducer equivalent model of a TEG (adapted from [54]).

Assuming that there is no contact resistance between each plate and the legs, the applied temperature difference in the plates is equal to the one at P and N legs; that is,

$$\Delta T' = T'_H - T'_C = \Delta T = T_H - T_C. \tag{4.3}$$

The associated DC source is constant and equal to $\alpha\Delta T$, so the Open Circuit Voltage (OCV) becomes

$$V_{OC} = \alpha\Delta T; \tag{4.4}$$

and the output voltage is

$$V = \alpha\Delta T - R_E I. \tag{4.5}$$

It should be noted that α depends on the TEG internal material, while ΔT depends on the operating conditions. Then, considering Equations 4.4 and 4.5, the power delivered to a load, R_L, becomes

$$P = \alpha(T_H - T_C)I - R_E I^2, \tag{4.6}$$

$$P = V_{OC} I - R_E I^2. \tag{4.7}$$

Using Equations 4.5 and 4.7, *V-I* and *P-I* characteristic curves are constructed and presented in Figure 4.5. There is one point where the TEG delivers the maximum power. This operation point is known as the Maximum Power Point (MPP). The set of curves, *V-I* and *P-I*, is used to determine the corresponding MPP [55].

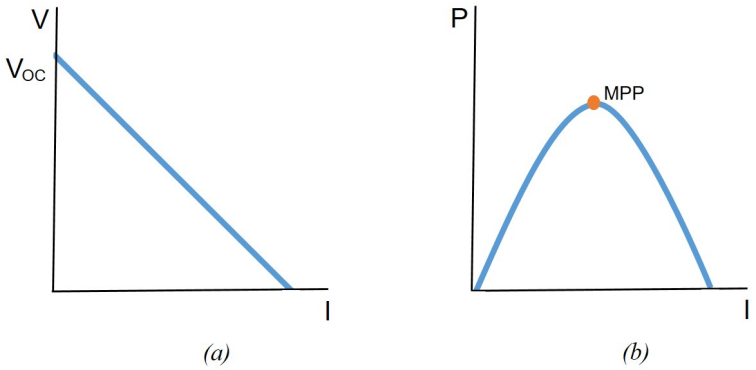

Figure 4.5: TEG characteristic curves (adapted from [54]). *(a) V-I* curve *(b) P-I* curve.

With the simplest model presented in Figure 4.4, the MPP can be found from the derivative of Equation 4.7 as

$$\frac{dP}{dI} = \frac{d}{dI}(V_{OC}I - R_E I^2), \tag{4.8}$$

$$\frac{dP}{dI} = V_{OC}I - 2R_E I = 0. \tag{4.9}$$

Then, solving Equation 4.9 for I

$$I = I_{MPP} = \frac{\alpha\Delta T}{2R_E}, \tag{4.10}$$

the MPP voltage and power are obtained from Equations 4.10, 4.5 and 4.7, as

$$V_{MPP} = \frac{\alpha\Delta T}{2}, \tag{4.11}$$

$$P_{MPP} = \frac{(\alpha\Delta T)^2}{4R_E}. \tag{4.12}$$

4.3 Phase Change Materials

Phase change materials are substances that storage latent heat of fusion. They exchange large amount of heat through a change in their physical state [56]. The thermal energy transfer occurs during solid–liquid or liquid-solid phase changes.

Unlike sensible storage materials, PCM storage systems have the advantage that they operate with small temperature differences during the phase change while storing or releasing thermal energy. They can store 5–14 times more energy per unit of volume than sensible storage materials such as water, masonry, or rock [57]. Figure 4.6 presents the T-Q characteristic curve. The phase change temperature remains constant in a value of T_{PC} while exchanging an amount of heat of $Q_f - Q_i$.

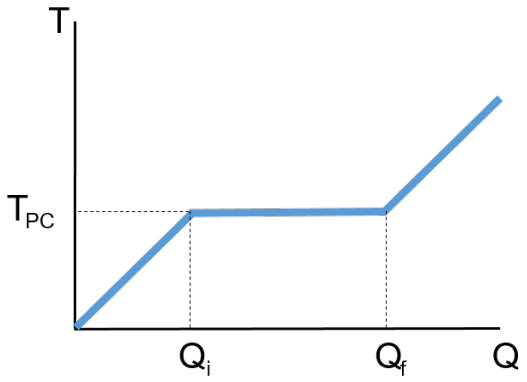

Figure 4.6: PCM T-Q characteristic curve (adapted from [58]).

PCMs are also used as thermal stabilizers due to the property of maintaining their temperature constant during the phase change. For this thesis, the use of low-T_{PC} PCM is evaluated to keep the cold TEG plate temperature within the desired range.

4.4 Solar Panel

Solar energy is used to generate electricity directly from solar radiation using photovoltaic (PV) effect. The conversion of solar energy into electricity is developed in a solar panel, a solid state-device composed of PV cells. A PV cell consists of a junction between two thin layers (N-type and P-type) of a doped semiconductor material whose electrical behavior is altered with tiny quantities of an impurity. This produces a *surplus* and a *deficit of free electrons* in the N-type and the P-type materials. To obtain more power from PV cells, groups of them are connected in series or parallel in a solar panel [59]. Despite the majority of cells are silicon-based, they are divided into three main categories: monocrystalline, polycristalline and amorphous. Crystalline SPs are commonly used for outdoor applications while amorphous are used for indoors.

Several physical effects are considered on the electric generation of a solar panel: the light generated current, the movement of current through the cell, contact resistance between the metal contacts and the silicon, and manufacturing defects [60]. The electrical model is constructed using linear and non-linear elements. A current source characterizes the

light generated current, a series resistance is used to describe the power losses due to contact resistance and a shunt resistance models the losses due to manufacturing defects. A diode is used to model the solar cell behavior in the dark [61]. Figure 4.7 shows the described equivalent model.

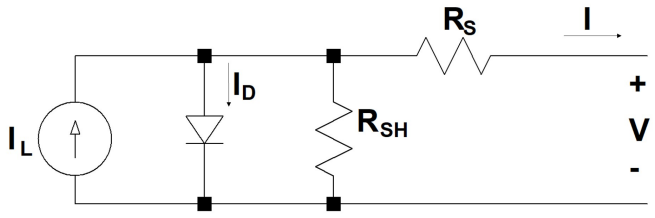

Figure 4.7: SP electrical model (adapted from [62]).

Applying circuit analysis techniques, the relation between current and voltage of a SP is given by

$$I = I_L - I_O(e^{\frac{V+IR_s}{nV_T}} - 1) - \frac{V + IR_S}{R_{SH}}, \tag{4.13}$$

where I and V are SP current and voltage, I_L is the light generated current, n is the amount of cells connected, V_T the thermal voltage, R_S the series resistance and R_{SH} the shunt resistance. From semiconductor theory, V_T is defined as

$$V_T = \frac{KT}{q}, \tag{4.14}$$

with $K = 1.38 * 10^{-23} J/K$, $q = 1.6 * 10^{-19} C$ and T the temperature in K.

Given the temperature and environmental conditions dependence, modeling and tests are made considering the following Standard Test Conditions (STC) [63]:

- Cell temperature of 25°C.
- Radiation of 1000 W/cm^2 (known as one-sun of illumation).
- Air mass 1.5.

Considering that the module exhibits dependence on radiation and temperature, light generated current I_L can be expressed as

$$I_L = G\left[I_{L,STC} + k_i \Delta T\right], \tag{4.15}$$

where G is the ratio of current radiation to STC radiation, k_i the temperature coefficient and ΔT, the difference between current temperature and STC temperature. Based on the connected load, the electrical operation is described. When the resistance is infinite, the current in the circuit is at its minimum and the voltage is known as Open Circuit Voltage (OCV or V_{OC}). In contrast, when the resistance is zero, the current reaches its maximum and is known as the Short Circuit Current (I_{SC}). Varying the resistance from 0 to ∞, the *I-V* characteristic curve is constructed as in Figure 4.8 *(a)*, presenting the MPP.

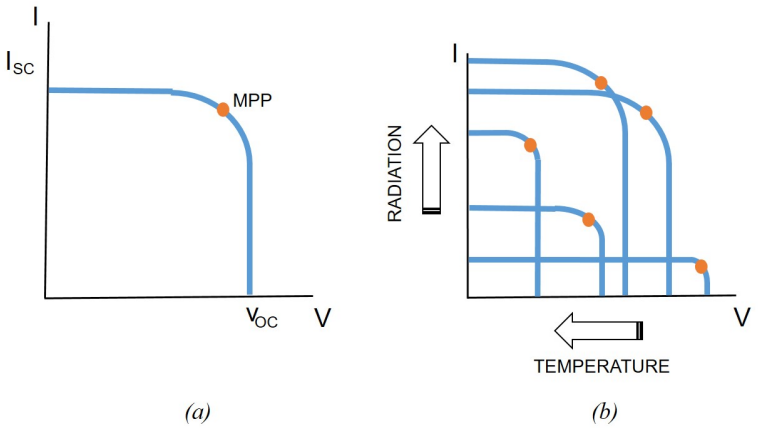

Figure 4.8: Theoretical *I-V* curves for SPs (adapted from [64]). *(a)* I-V curve *(b)* Variation on I-V curve due to radiation and temperature increasing.

The efficiency of a SP is defined as the percentage of the solar energy falling on its surface that is converted into electrical energy. It is associated with the building materials and is affected by the operating conditions [65]. Taking into account the radiation levels and cell temperature, a SP does not present a single characteristic curve. This varies with the ambient temperature, humidity, dirt, shade, angle of incidence, among other external variables. Figure 4.8 *(b)* shows the change that occurs in the characteristic curve; and therefore, in the MPP, as temperature and radiation vary. It should be noted that an increase in the radiation received causes the MPP to increase, while an increase in temperature causes the MPP to decrease. Consequently, the MPP operation becomes critical to obtain the maximum electricity from the SP.

4.5 Power Management Unit

The output power from any supply system can be varied according to the connected load. As the load changes, the supply system must be capable of providing sufficient amount of power. Therefore, many DC power supply designs require, within many features, a regulated output for its operation [66] . Regulated power supplies maintain the voltage

constant at the output terminal while varying the load currents. DC-DC converters are circuits that convert a DC voltage to a different DC regulated level [67] . Output voltage can be lower or higher than the input depending on the configuration.

Linear regulators are simple way of converting a DC supply voltage to regulated lower DC voltage. The circuit of Figure 4.9 shows a linear regulator which uses a transistor as a variable resistance [68].

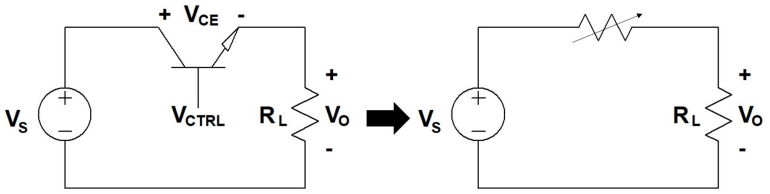

Figure 4.9: A basic linear regulator (adapted from [68]).

By adjusting the transistor base current, the output voltage may be controlled over a range of 0 to *Vs*. The output voltage is defined as

$$V_o = I_L R_L, \tag{4.16}$$

where the load current (I_L) is controlled by the transistor (V_{ctrl}). However, the power loss in the transistor causes this circuit to present a low efficiency. Therefore, **switching converting circuits** are proposed as an efficient alternative to linear regulators [67].

In a switching converting circuit, the transistor on Figure 4.9 operates as an ideal electronic switch by being completely on or off. The output voltage is the same as the input when the switch is closed, and the voltage is zero when the switch is open. The result is a periodic opening and closing of the switch [68]. The duty ratio (D) is defined as the ratio of the open time and the switching period. The switch is closed for time DT and open for $(1 - D)T$ [69]. The definition is presented in Equation 4.17.

$$D \equiv \frac{t_{on}}{t_{on} + t_{off}} = \frac{t_{on}}{T} = t_{on} f. \tag{4.17}$$

As a consequence, the DC component (Eq. 4.18) is controlled by adjusting D as

$$V_o = \frac{1}{T}\int_0^T v_o(t)dt = \frac{1}{T}\int_0^{DT} V_s dt = V_s D, \tag{4.18}$$

being f the switching frequency. From Equation 4.17, the duty cycle is always less than 1, and from Equation 4.18 the DC component is be less than or equal to the input

voltage of the circuit. The power absorbed by the ideal switch is zero, but losses occur in a real switch.

Switching converting circuits are useful in applications which do not require a constant DC source. To obtain average values from a basic switching converter, an inductor-capacitor (L-C) low pass filter is added after the switch, as shown in Figure 4.10 *(a)*.

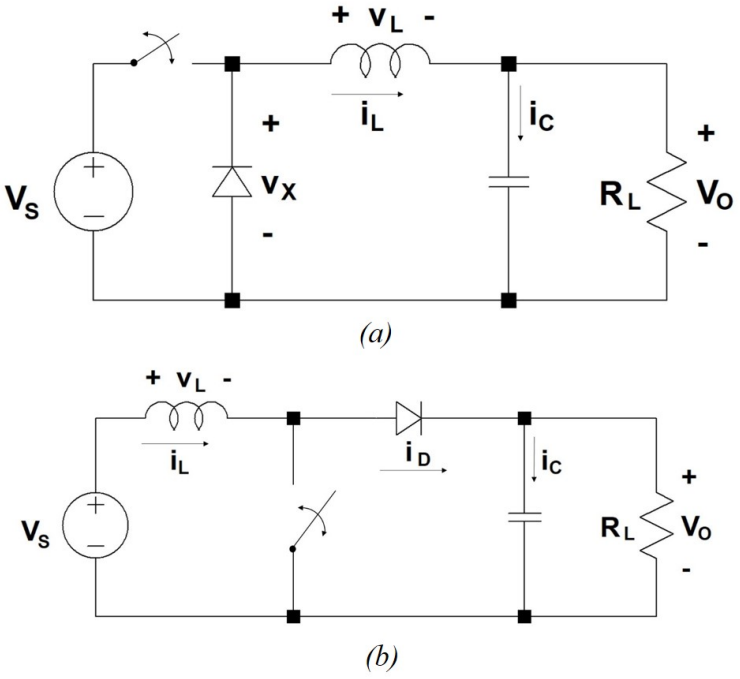

Figure 4.10: DC-DC converters (adapted from [68]). *(a)* Buck converter *(b)* Boost converter

Also a diode is included to provide a path for the inductor current only when the switch is opened. The output voltage is less than the input, so this circuit is called a **buck converter** or a down converter [70].

For the purpose of this approach, it is required a DC-DC converter with an output value larger than the input [71]. A **boost converter** is another switching converter with (L-C) filter that operates periodically opening and closing an electronic switch but steps up the voltage [72]. Figure 4.10 *(b)* shows a boost converter.

To analyze the operation of the boost converter, voltage and currents should be studied. Nevertheless, Equation 4.17 and the following assumptions must be taken into account:

- The circuit has reached its steady state.
- The inductor current is always positive and periodic.
- The average inductor voltage is zero.

- The capacitor is very large.
- The average capacitor voltage is zero.
- The output voltage is held constant at V_o.
- The power delivered to the load is the same as the power supplied (ideal components).

With those assumptions, the output voltage is

$$V_o = \frac{V_s}{1 - D}. \tag{4.19}$$

According to Equation 4.19, if the switch is always open and D is zero, the output is the same as the input. But if the denominator becomes smaller, the output becomes larger than the input. The output is never less than the input. Equation 4.19 is based on the assumption of ideal components. However, the minimum combination of inductance and switching frequency for to maintain a continuous current in the boost converter is

$$L_{min} = \frac{D(1 - D)^2 R}{2f}. \tag{4.20}$$

Furthermore, a non-ideal capacitance results in a ripple at the output voltage. The peak to peak output voltage ripple can be calculated as

$$\frac{\Delta V_o}{V_o} = \frac{D}{RCf}. \tag{4.21}$$

4.5.1 Maximum Power Point Tracking

As SP and TEG output power changes with irradiation and temperature, performing a search of the MPP is also mandatory; so that, total supply efficiency is further maximized [73]. Maximum Power Point Tracking (MPPT) permits to obtain the maximum power available from non-linear electrical power sources. In a EH system, tracking is done in the power management unit (DC-DC converter). To maintain the source on its MPP, the duty cycle of the converter is varied. MPPT tackles a set of techniques such as Perturbate and Observe ($P\&O$), Incremental Conductance (IC), Parasitic Capacitance (PC) and Open Circuit Voltage [74, 75].

$P\&O$ method changes the source voltage causing a perturbation every single cycle. It is the simplest method because does not need a-priory information about the source.

Voltage and current measurements are used to calculate the output power and compare with previous state. There is an increase in the duty cycle if the power decreases when the voltage increases, and there is a decrease in the duty cycle if the power increases and the voltage decreases [76]. Tracking is done following the perturbation. However, the output voltage oscillates around MPP, generating a power loss.

The method *IC* does not require a-priory information either. This technique consists of varying the voltage according to MPP by changing the instantaneous conductance. It can track quicker than *P&O*, but it is more complex to implement. Similarly, *PC* considers a parasite capacitance in the SP and with that information tracks MPP. It is used in large SP arrays [77]. Constant voltage methods assume that the operating voltage at the MPP does not vary significantly. In SP, MPP voltage is usually considered as 0.76 times the *OCV* [78]. However, this method does not consider rapid changes in radiation. According to Equation 4.11, MPP voltage is considered half the *OCV*. Consequently, this method result effective for TEG because of the low change percentage in the MPP [79].

4.6 Storage Units

4.6.1 Batteries

Batteries are entities that convert the chemical energy directly into electric energy in an electrochemical reaction. They are composed of one or more basic electrochemical units (cells) connected in series or parallel according with the desired output voltage and capacity. Each cell contains a negatively charged electrode (anode), a positively charged electrode (cathode) and a ionic conductor (electrolyte).Figure 4.11 *(a)* presents a battery with its internal components.

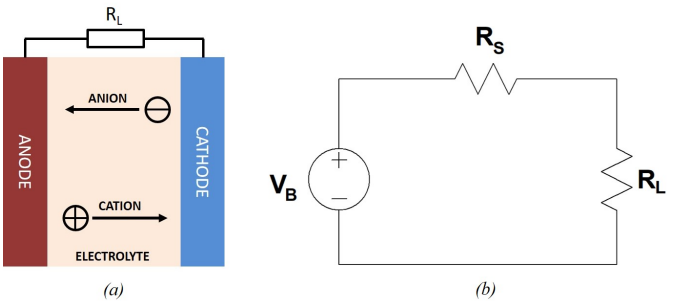

Figure 4.11: Battery (adapted from [36]) *(a)* internal components *(b)* electrical model.

Charge transfer is made between anode and cathode via ions (anions and cations), being the electrolyte its mean. The electrical model of a battery is shown in Figure 4.11 *(b)*.

It contains a voltage source (V_B) which characterizes the OCV. V_B depends on the used materials and stored charge (Q). While Q decreases, V_B also decreases. Then, a series resistance (R_S) models the equivalent resistance. Its value depends on the chemistry, battery design and temperature.

Batteries are classified as primary or secondary according to the capacity of being recharged. **Primary batteries** are a preferred option for long duration, low-discharge current applications. Their lifetime can span from 3 to 20 years, but cannot be electrically recharged. As a result, they must be replaced when depleted. The manufacturers provide a discharge curve with a specific resistance as load to analyze their capacity. It is defined as the total electrical charge that can be drained from a fully charged battery and represents the number of hours that the battery can power a certain load [80]. The lifetime is defined as the time required for the battery to self-discharge due to unwanted chemical reactions while stored on the shelf. Also, the Depth of Discharge (DoD) measures the amount of energy extracted from the battery compared to its capacity. Primary batteries are grouped in four categories based on their chemical composition [81]:

- Alkalines.
- Lithium based.
- Zinc-air.
- Silver-oxide.

Alkaline batteries are used in everyday applications (remote controls and toys) for their low cost. However, lithium based batteries provide higher voltages, energy density and lifetime. In contrast, zinc-air and silver-oxide batteries have high internal impedance, making them unsuitable for autonomous sensors.

Secondary batteries are used for portable devices because they can be electrically recharged easily. The lifetime is defined as the number of charge/discharge cycles at 80% of its original capacity. They have higher initial cost, lower energy density but maximize the cycle life. Secondary batteries can be divided in two main categories [81]:

- Lithium based (Li-ion or Li-Polymer).
- Nickel metal hydride.

Both categories require protection circuits due to their sensibility to overcharge and over-discharge. However, among secondary batteries, Li-ion have the highest cycle life lowest internal impedance and self-discharge percentage.

4.6.2 Supercapacitors

Supercapacitors (or ultracapacitors) are often used for auxiliary applications. They have higher capacities per unit area than that of a regular capacitor due to their large superficial area compared to the molecular range. Its structure is shown in Figure 4.12 *(a)*. Instead of having a dielectric between their plates, an ion absorption layer permits the charge/discharge via ions [82]. The electrical model of a supercapacitor is presented in Figure 4.12 *(b)*, where C is the nominal value of the capacitor, R_C is the equivalent series resistance, and R_{LEAK} represents the leakage current. This current passes through a parallel resistance once the capacitor has been fully charged. The resistors R_C and R_{LEAK} are relatively large causing a voltage drop and low leakage [83].

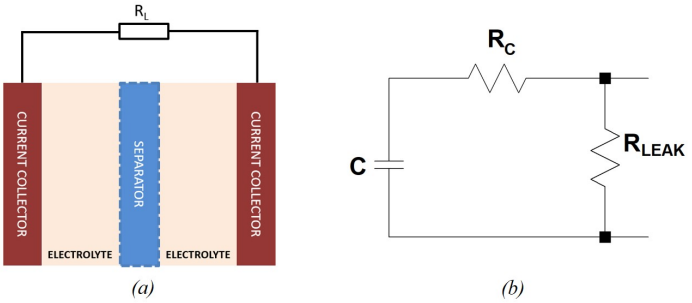

Figure 4.12: Structure of a supercapacitor (adapted from [84]).

Table 4.2 compares secondary batteries with supercapacitors. Supercapacitors energy densities are one or two orders of magnitude lower than secondary batteries but present lower series resistance, causing them to be more expensive.

Table 4.2: Comparison between secondary batteries and supercapacitors [36].

Feature	**Secondary battery**	**Supercapacitor**
Energy density $[mWh/cm^3]$	100-500	1-10
Series resistance	Tens to thousands of $m\Omega$	Units of $\mu\Omega$ - Hundreds of Ω
Leakage	No	Yes
Temperature range [K]	253.15 to 333.15	253.15 to 353.15
Cycle life [cycles]	300 to 1000	100000

Chapter 5

Related Work

One of the tendencies to favor connectivity and information sharing among people and entities is the transformation of regular cities into *smart cities*. The principle of enabling physical objects to share information and make decisions without human interference can be used strategically to manage urban spaces [85]. Therefore, remote sensing emerge as the key element in the structure of the smart city environment. To guarantee such transformation, it is required a continuous operation of sensors and devices that transfer the information to a platform such as the Internet. Energy harvesting is proposed as an alternative to power low-power devices up with ambient energy sources. Thermoelectric energy harvesting uses the remaining thermal energy to produce electricity via TEGs [86]. As a result, a TEG can be excited by the thermal energy of any process that produces a temperature difference.

A study of TEH for an industrial temperature sensor is found in [87]. First, a TEG module is characterized based on a finite element analysis model. The authors use a heating device with adjustable temperature range, which reaches maximum temperature gradients of 16K. With the TEG excited, a boost converter is used to manage the power required for sensors. The output voltage of the thermoelectric module ranges around 35mV and 107mV, and 0.19mW to 1.51mW of output power. In [88], the authors propose a thermoelectric energy harvesting system to run a microcontroller unit and a wireless sensor node. The energy source is the difference between a controlled temperature heater and a heat sink based on water. The prototype produces a minimum thermoelectric open-circuit voltage of 62 mV and a minimum output power of 84 μW. Both prototypes (from [87] and [88]) require a temperature control mechanism for the cold side.

The energy produced by industrial processes that involve ovens and boilers at high temperatures can be used for EH. In [89] the authors use a gas heater as a heat source and obtain enough electric power to charge a cell phone while cooking. The hot side

of the TEG is on a conductive sheet in direct contact with the heat source, while a metal heat sink is used on the cold side to maintain its temperature. A low input DC-DC converter is connected to the terminals of the TEG to maintain the constant voltage in the USB charger output. Thus, an average output power of 7.3W is achieved with a temperature difference of 270K. That amount of power permits to maintain the temperature on the TEG cold side with a cooling fan and still deliver power to the load. However, this represents power losses because the TEG is being used to power the fan. Also, a large heat sink is required to maintain the temperature at desired levels.

Some approaches have also shown that changes in ambient temperature and the incidence of solar rays on the surface produce temperature differences in a thermoelectric material. As a result, it is possible to provide energy to low-power environmental sensors. In [90], a self-powered wireless sensor node for temperature measurement is presented. The device is powered by a thermoelectric generator exposed to the ambient light. Temperature differences less than 15K are achieved. The output power directly depends on maintaining the cold side at ambient temperature, and that work reports the use of a 52x35mm^2 metal heat sink for this purpose. With the selected temperature difference, a maximum power of 500μW is harvested, which allows a maximum backup charging time of 6h.

Another self-feeding temperature sensor is presented in [91]. Temperature differences between the exterior and interior of a bedroom are used as a source of heat. The authors create a model to estimate the available power using historical climate data and to compare the real power delivered to the sensor. The room temperature is held constant at 295.15K (22°C) with the air conditioner. In a summer day, the harvester delivers an average output power of 28.7 μW, enough to charge a supercapacitor and power a sensor node with periodic temperature measurements and transmissions.

In [92], a 4-TEG harvester for WSN is presented. It maintains a temperature gradient of 3K using ambient temperature as heat source. The TEH contains a cold temperature control mechanism, which consists of a DC-motor water pump that requires an external power source. Despite of the fact that they theoretical explore the possibility of using PCM, the system is fabricated and implemented using water as thermal stabilizer.

In [93], variations in atmospheric temperature in a climate cabin are used to produce a maximum temperature difference of 31K in a TEG module. The prototype produces a maximum average power of 6mW and an overall energy conversion efficiency of 89% with the DC-DC converter installed.

Pavements and streets also increase their temperature during the day while they are exposed to solar radiation [94]. In [95], the authors present advances on the development

of pavement thermoelectric technology. They study temperature differences produced by the incidence of sun rays in pavements and ambient air to excite road thermoelectric generators (RTEG). Using 0.9 cm^2 RTEGs an output voltage of 0.4V is produced when the temperature difference is 15K in winter. In summer, the output voltage is about 0.6–0.7 V, with a temperature difference of 25–30K. In tropical and subtropical regions, larger temperature differences can be achieved [96].

Given the demonstrated potential of the TEGs, an array of multiple TEGs allows to increase the power delivered by an TEH system. In [97], the authors propose a prototype that consists of an array of 12 TEGs connected in both series and parallel. The hot plate of the TEG is exposed directly to the incidence of solar rays, while the cold plate is on cold water, acting as a heat sink. For both arrays, series and parallel, average powers of 1.23W and 0.43W were obtained, respectively. When comparing the power of the 12 TEG array with 4 TEG under the same conditions, the power increases by 96% for the array in series and 93.52% for the array in parallel. In [98], the authors present an autonomous multisensor system for agricultural applications. It is powered by a thermoelectric generator excited with the incidence of solar rays. To maintain the cold side temperature, an aluminum heatsink is used achieving a maximum temperature of 308K and maximum TEG voltage of 200mW with 8K of temperature gradient. A low voltage DC-DC converter charges a 1.65F supercapacitor.

One of the main disadvantages of using TEG as transducer is that it is necessary to maintain the temperature difference to guarantee a greater conversion from thermal to electrical energy. The incidence of solar rays is considered a hot temperature source for TEG. This implies that the cold temperature must be maintained at appropriate levels. Some solutions presented before use heat sinks, fans and even materials with dissipative properties such as water. However, this increases the total area required for the EH system. In addition, they are considered impractical solutions if desired to implement in remote sensing. PCM keep their temperature constant during the phase change; therefore, it is possible to use them as thermal stabilizers [99]. In [100], the authors confirm the potential of the application of PCM as a cooling/heating media in TEGs. They use a PCM with a melting temperature of 303.5K. During phase change, cool side temperature increases by only about 1–1.5K, achieving maximum output voltage of 0.35V with 45mA current.

In [101], a double stage TEH with PCM is proposed. In the first stage, a TEG module installed between a PCM heat sink, as cooling system, and an the heat source. Because of the inherent characteristics of PCMs to save the thermal energy as latent heat, the PCM heat sink is used as the heat source of the second stage TEGs. Five smaller TEG modules are installed around the PCM with individual heat sinks for cooling with natural

convection. The second stage achieves maximum temperature differences of 100K, while the first stage only achieves 87K. The results show the proposed TTEG system averagely generates 27% more electrical potential than the one-stage TEG system. However, the experiment is carried out with a laboratory heating device as heat source. For the case of remote sensing, it required to evaluate if those temperature gradients are reached.

Hybrid collection systems also extend the life of WSN. In [102], a double source energy harvesting circuit is proposed. The authors demonstrate the integration of energy extracted from a piezoelectric transducer and a thermoelectric generator. The PZT is tested with a shaker and the TEG is modeled as a DC source with a series resistance. The results show that the hybrid systems provide output voltage ranges of 3-4V delivering 450uW of power. Also, PV-TEG hybrid systems are commonly used. With the principle that solar energy absorbed by the PV cell is not only converted into electrical energy, but in thermal, they pretend to improve the output power combining two transducers. Thermal energy from the PV module is then utilized by the TEG. In [103], the authors propose an alternative to improve the performance of a hybrid PV-TEG system. The TEG is placed below an amorphous PV cell and the ceramic plates are eliminated to enhance the heat transfer. To maintain the temperature differences, a recipient with a mixture of ice and water is installed on the TEG cold side finding an average output power of 21.60mW only for the TEG, and a maximum average power of 40mW for both sources. However, the system presents efficiencies lower than 10%.

Finally, in [104] a hybrid energy harvesting system based on a solar panel and a TEG arrangement using a parabolic dish solar concentrator is proposed. It is found by the authors that the system is 38.65% more efficient than one that only contains solar panels under solar concentration. However, the concentration scheme produces an undesired increase on the solar panel temperature and the efficiency decreases.

Chapter 6

Proposed Approach

In this chapter, the methodology and proposed approach are exposed. First, transducers used for the development of this research are characterized; that is, one commercial TEG and one commercial SP of comparable size. Subsequently, the operating conditions of the TEH scheme are established and its main components are explained. Finally, the scalability of the scheme is evaluated using arrays of 2-TEG, 3-TEG and 4-TEG.

6.1 Characterization of Energy Transducers

Since the principle of TEG operation involves heat and electricity, the first step in the process of using a TEG as an energy source comes with its characterization. This permits to propose an equivalent electric model that can be used for simulations; so that the analysis, design and performance evaluation with other electric components can be carried out using SPICE-based software. To make a fair comparison with the performance of TEG, a commercial SP with similar area is also characterized.

6.1.1 Thermoelectric Module TEC-12706

Two commercial thermoelectric generators, SP1848 [105] and TEC-12706 [106], are considered for the TEH prototype. Both modules present $16cm^2$ of area. According to the manufacturer, the Seebeck coefficient is 53mV/K for TEC-12706, while only 22.22mV/K for SP1848. Considering that the voltage is directly proportional to the Seebeck coefficient; that is, at greater α more power is obtained, TEC-12706 module is selected for characterization.

A design of experiments is proposed to validate the TEG electrical model presented in Figure 4.4. The purpose is to estimate the parameters involved on the transduction process. First, the TEG is tested at several temperature differences and measurements of OCV and temperature gradient are taken to estimate the Seebeck coefficient from Equation 4.4. The voltage is measured with an Amprobe 37XR-A multimeter. The cold side temperature is measured with a Fluke 80BK-a K-type thermocouple and the hot side temperature is measured with a Fluke 63 Mini Infrared Thermometer. A metal plate is placed on top of the TEG hot plate and is excited with a heat gun. To maintain the cold plate temperature, a heatsink with a cooling fan is installed. Figure 6.1 shows the testbench configuration.

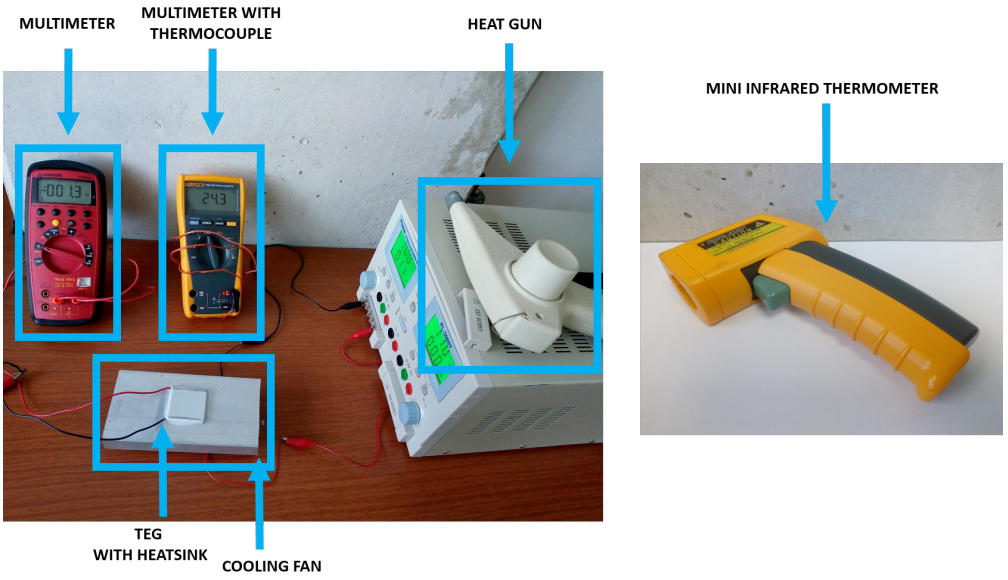

Figure 6.1: Experiment configuration from TEG parameters estimation

The temperature gradient is calculated according to Equation 4.3. The experiment evaluates temperature differences of 20K, 30K, 40K and 50K; and for each temperature difference, 200 measurements are taken. The Seebeck coefficient is experimentally calculated using Equation 4.4, finding an average α of 52.738mV/K with a standard deviation of 1.976mV/K. With confidence intervals of 95%, the true mean Seebeck coefficient is between 52.592 mV/K and 52.885mV/K.

Then, it is necessary to validate estimate the TEG series resistance. According to Figure 4.4, the output voltage can be expressed using a voltage divider as

$$V_O = \frac{R_L}{R_L + R_E} V_{OC}. \tag{6.1}$$

Thus, solving Equation 6.1 for R_E, the series resistance is

$$R_E = \frac{V_{OC} - V_O}{V_O} R_L. \tag{6.2}$$

Measurements of output voltage, current and temperature gradient are taken for a fixed 1Ω load. This selected value in based on an estimated value of the series resistance provided by the manufacturer according to the semiconductor material of the TEG [106]. The actual series resistance can deviate from the given specification when considering contact resistances between the semiconductor and the ceramic plates. The 1Ω-load resistance was chosen to match the theoretical series resistance and maximize the observed output power. Hence, the OCV is calculated with the previously estimated α and with 1.000 measurements of ΔT. Temperature gradients are varied from 10K to 50K with 10K steps. Then, using Equation 6.2, the average series resistance, R_E, is refined to 1.536Ω with a standard deviation of 0.033Ω. With confidence intervals of 95%, the true mean series resistance is between 1.534Ω and 1.538Ω.

Now, with the estimated α and R_E, it is possible to construct *V-I* and *P-I* curves as shown on Figures 6.2.

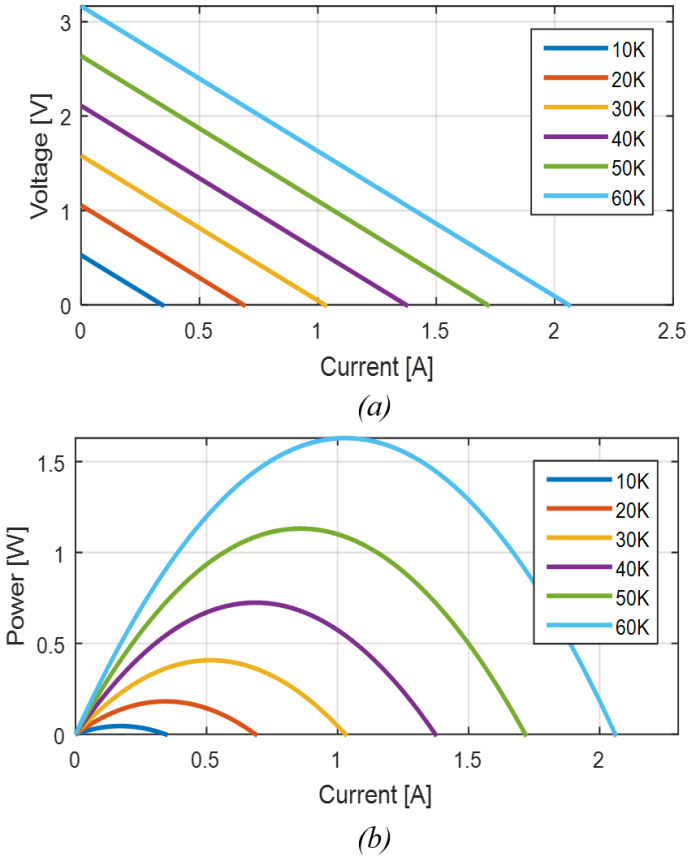

Figure 6.2: TEG characteristic curves constructed with validated parameters *(a) V-I* curve *(b) P-I* curve.

In addition to the V-I and P-I curves, the theoretical P-ΔT and η-ΔT are constructed (see Figure 6.3). These characteristics are important since it is expected to determine the operating conditions to propose the TEG as an alternative to the use of SP. According to Figure 6.3 *(b)*, for a target efficiency of 20% (good quality SP) a minimum temperature gradient of 26.31K is required. It should be noted that for efficiency calculations, it is used a radiation of $1000W/m^2$. This radiation corresponds to the STC used to evaluate the performance of SPs.

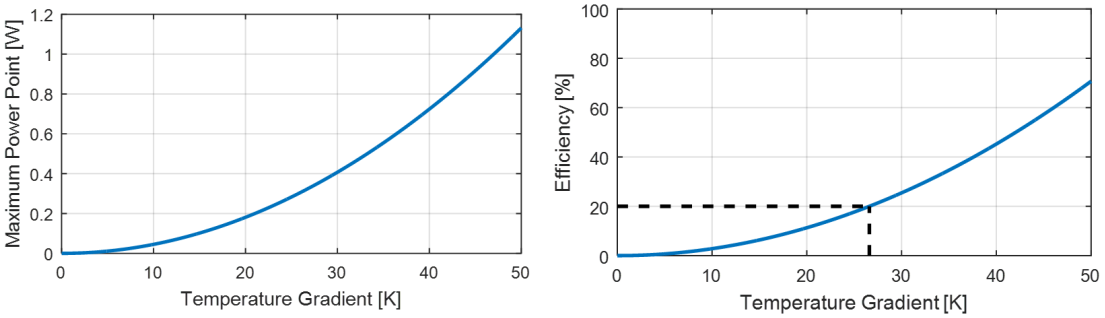

(a) *(b)*

Figure 6.3: Curves constructed for temperature gradient selection *(a)* MPP-ΔT curve. *(b)* Efficiency-ΔT.

6.1.2 Solar Module 2V-50mA

Two different commercially available solar panels are evaluated in Table 6.1. Both modules exhibit the same theoretical efficiency at STC and their output power is below 1W.

Table 6.1: Comparison between polycristalline SPs [107, 108].

Solar Panel	**Area** $[cm^2]$	P_m **[W]**	η [%]
5V-SP	80	0.8	14
2V-SP	20.25	0.1	14

The output power characteristic makes both of them suitable for powering an low-power device. However, the 5V-SP presents an increase of 400% of the TEG area while the 2V-SP presents only 26.56%. To make a fair comparison with the TEH system, the 2V-SP module is selected for characterization. Figure 6.4 shows the polycrystalline SP of 100mW. The main electrical specs are summarized in Table 6.2.

Unlike the TEG, the parameters of the electric model presented in Figure 4.7 for SP directly depend on the stochastic nature of radiation. Therefore, an experimental approximation of the model is impractical in an uncontrolled environment.

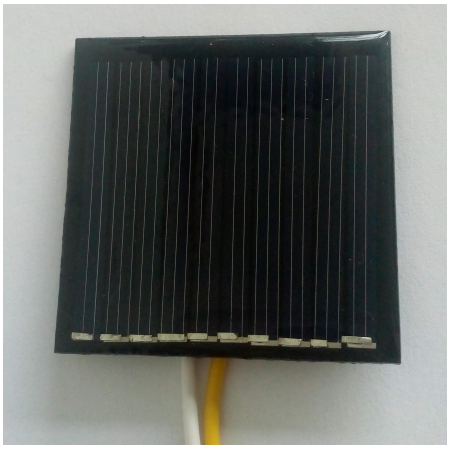

Figure 6.4: Selected SP for comparison.

Table 6.2: SP main parameters [107].

Spec	Value	Description
V_{OC}	2.2V	Open circuit voltage
I_{SC}	55mA	Short Circuit current
V_{MPP}	2V	MPP voltage
I_{MPP}	50mA	MPP current
P_{MPP}	100mW	Maximum power point
η	14%	Efficiency at STC

The parameters provided by the manufacturer are used to construct the *I-V* and *P-V* curves using the STC. Considering that the equivalent electrical model is defined by non-linear elements, the characterization is limited by the difficulties to solve Equation 4.13 using analytical models. Several algorithms have been developed for solving this equation with numerical techniques [109]. In addition, certain approximations are used to solve the non-linear equation. For example, Esram algorithm assumes that the slope of the *I–V* curve at V_{OC} and I_{SC} is controlled by the series and shunt resistance. With Newton-Raphson technique, the equations derived from the assumptions are solved to find the parameters of the equivalent model [110]. A method for finding R_S and R_{SH} is proposed in [111]. It is based on the fact that there is only one pair of resistances that satisfies the MPP. On the other hand, in [112], the authors use the coordinates of four arbitrary points of the characteristic *I–V* curve and their slopes to estimate the five parameters of the solar cell single-diode model. This method does not require numerical techniques but requires a priori information of the *I-V* curve.

For this approach, the superposition technique is used [113]. It consists on the assumption that I_L can be approximated to I_{SC}. Then, the *I-V* curve is the superposition of two curves. One of them is produced by the constant current source I_{SC} (see Figure 6.5 *(a)*), while the second one is the *I-V* curve for the diode considering two conditions.

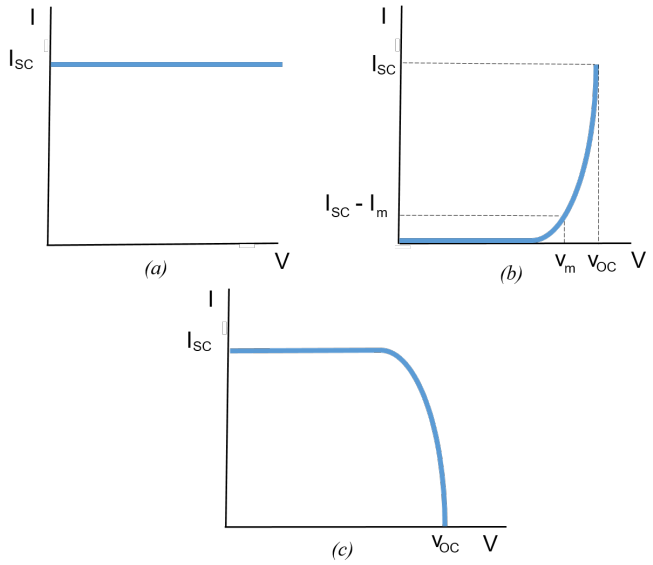

Figure 6.5: Approximation of the *I-V* characteristic curve (adapted from [113]). *(a)* Constant current source *(b)* Diode *I-V* curve. *(c) I-V* approximated curve.

First, that at V_{OC}, the current flowing by the diode is equal to I_{SC} (see Figure 6.5 *(b)*). Second, that at the MPP voltage, the current flowing through the diode is $I_{SC} - I_{MPP}$. As a result, the *I-V* curve becomes the one shown in Figure 6.5 *(c)*. The diode equations derived from the previous assumptions (Eq. 6.3 and Eq. 6.3) permits to obtain the remaining parameters of the model.

$$I_{SC} = I_o e^{\frac{V_{OC}}{nV_T}}. \tag{6.3}$$

$$I_{MPP} = I_o e^{\frac{V_{MPP}+I_{MPP}R_S}{nV_T}}. \tag{6.4}$$

Then, the *I-V* curve is constructed in Matlab using Equation 4.13 (see Figure 6.6).

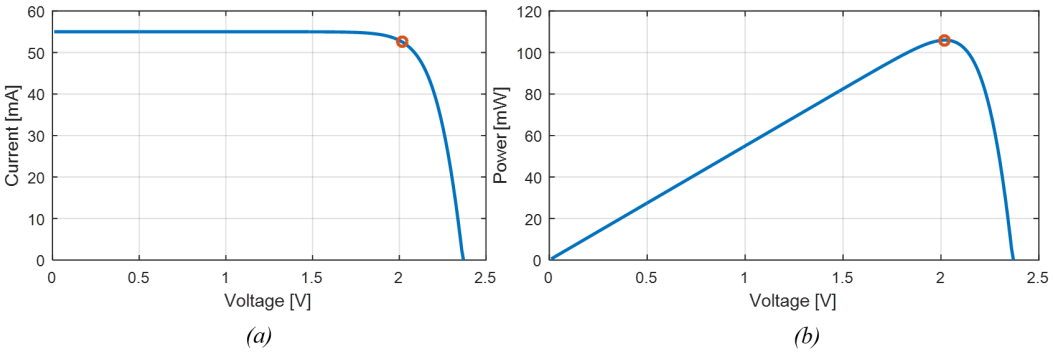

Figure 6.6: Approximated I-V characteristic curve (constructed in Matlab). *(a)* I-V curve *(b) P-V* curve.

The simulated conditions are summarized in Table 6.3. In addition, it includes the error percentages of the model according to the data delivered by the manufacturer. For all the simulated values, the error percentage is below 10%.

Table 6.3: Parameters of the approximation of SP model.

Spec	Simulated value	Error Percentage [%]
V_{OC}	2.37 V	7.72%
I_{SC}	54.9 mA	0.18%
V_{MPP}	2.01 V	0.5%
I_{MPP}	51.7 mA	3.4%
P_{MPP}	104.3 mW	4.3%

6.2 Establishment of TEG Operating Conditions

For this work, it is proposed to use the sun as energy source that provides the heat gradients for the TEG. Thus, characterization of the solar radiation pattern is important for the development of the unit. This experiment is carried out in the city of Barranquilla, Colombia (LAT 11.0 N, LONG 74.8 W), and according to agencies worldwide, the energy potential of the geographical area to about 6 PSH [13]. Also, according to the results presented in Section 2.1, the highest radiation estimates are present in Ranges V and VI, which are the targeted hours for TEH. To improve the heat concentration from the solar rays, a metal plate of $16cm^2$ is attached to the TEG hot side (see Figure 6.7).

(a) *(b)*

Figure 6.7: Metal plate for TEG hot side. *(a)* Metal plate. *(b)* TEG with metal plate.

Thus, temperature measurements are taken each two minutes from 9AM to 3PM during five days, according to the selected ranges. The days were chosen in the same week without considering the climatic conditions of each day. A Fluke 80BK-a K-type thermocouple is used for this purpose. Figure 6.8 shows the temperature increasing during the selected ranges when the metal plate is excited by the sun rays.

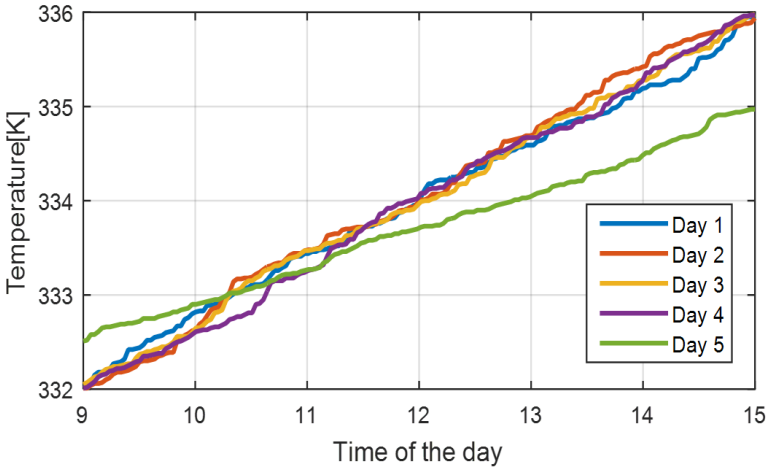

Figure 6.8: Hot plate temperature during the day.

Then, it is found that the average temperature is 334.017K(60.867°C) with a standard deviation of 1.132K. Also, Table 6.4 presents average temperature, standard deviation and confidence intervals for each day.

Table 6.4: Confidence intervals for *mean* hot temperature.

Day	Mean	Stnd. deviation	Lower limit	Upper limit
1	333.995	1.07009	333.838	334.153
2	334.058	1.18444	333.883	334.232
3	334.01	1.13229	333.843	334.176
4	333.974	1.17535	333.801	334.147
5	333.704	0.704167	333.6	333.807

It is important to note that the hot plate temperature does not require any type of mirror and/or magnifying glass. For the cold plate, it is required to set a minimum temperature up to 307.70K (34.55°C) given the measurements presented in Figure 6.8 and the expected efficiency of Figure 6.3. Thus, with lower cold side temperatures, the TEG output power can provide a TEG efficiency higher than 20%. The goal is to show that the TEG minimum efficiency is at least as good as high-quality SPs.

The challenge is that given the natural conduction between the TEG hot and cold plates, there exists the tendency of the cold-plate temperature to increase if it is not well regulated; which in turns decreases the temperature difference; and therefore, the power delivered by the module.

Thus, it is necessary to establish a mechanism to keep the temperature difference at the expected values maintaining the expected available power. Even though cooling fans or other active strategies can be used, the power drawn from the TEG makes this approach not energetically appealing for low-power applications.

A particular dissipative material must be attached to regulate the cold plate at the required temperature to maintain ΔT, but the advantage in this thesis is that such temperature regulation is obtained by passive means such as phase change material, as envisioned in Section 4.3. The use of PCM in this work is described in Section 6.2.1. Table 6.5 summarizes the estimated parameters associated with the TEC1-12706 and its expected operating conditions.

Table 6.5: TEG main parameters [106].

Parameter	Value	Description
Area	$16cm_2$	Dimension of the TEG
A	52.592mV/K	Seebeck coefficient
R_E	1.536 Ω	Electrical Resistance
ΔT	30K	Temperature gradient

6.2.1 Phase Change Material Preparation

Considering that is required to maintain a maximum cold side temperature of 307.70K, a commercial paraffin wax is used as thermal stabilizer. It presents a melting point range of 302.15 (29°C) – 309.15K (36°C). The main properties delivered by the manufacturer are summarized in Table 6.6.

Table 6.6: PCM main properties [114].

Properties	Value
Melting point [K]	302.15 - 309.15
Heat store capacity [kJ/kg]	160
Specific heat capacity [kJ/kg*K]	2
Density solid [kg/l]	0.86
Density liquid [kg/l]	0.77

One of the main disadvantages of using this material is the volume expansion during its phase change. The volume increases approximately 10% from solid to liquid. As the PCM is located below the TEG, there is a possibility that the PCM does not adhere to the TEG cold plate, because of the gravity effect, and the cooling mechanism does not work. Consequently, it is proposed to encapsulate the PCM in a metal cube.

Also, to guarantee that the cold side temperature does not surpass the limit for minimum efficiency; that is, the PCM does not surpass the melting temperature, a volume of $64cm^3$ of PCM is encapsulated. For this purpose, the PCM is placed in solid state in a beaker. Afterwards, it is melted in a laboratory water bath and the liquid is placed completely in the container (see Figure 6.9).

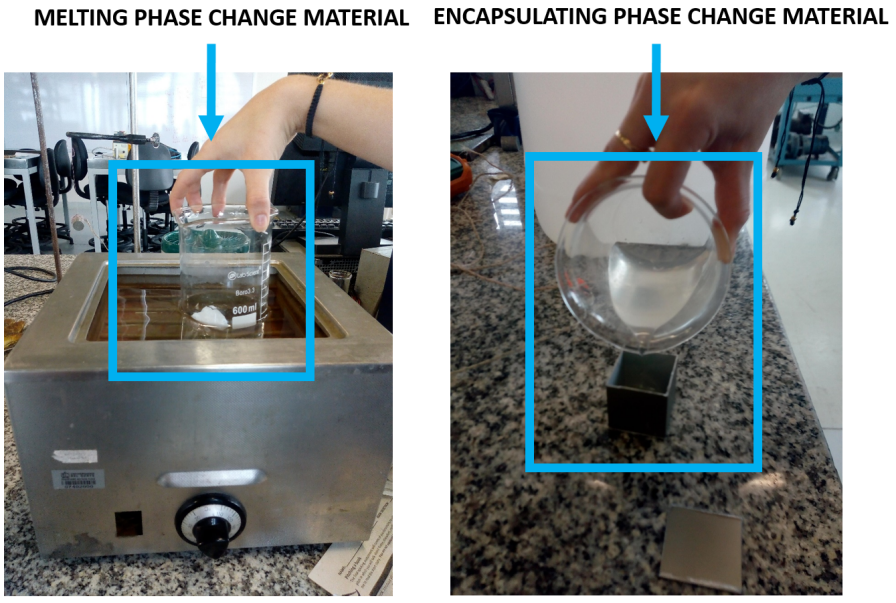

Figure 6.9: PCM encapsulating preparation *(a)* Laboratory water bath *(b)* PCM in liquid state.

When the PCM solidifies, the encapsulation is sealed. A total amount of 55g of PCM is placed inside a cubic container located under TEG as is presented in Figure 6.10.

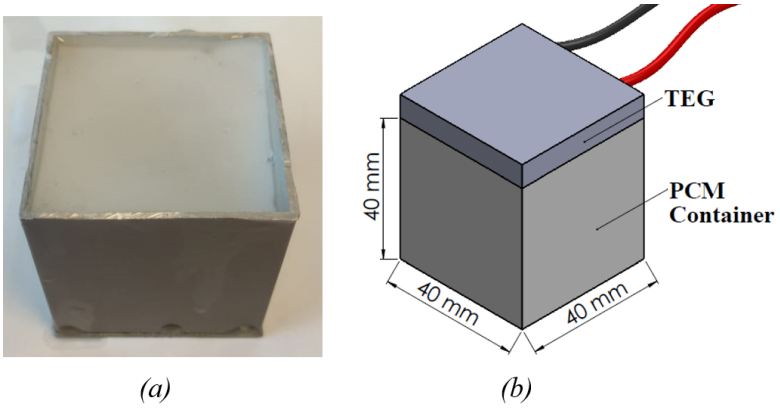

Figure 6.10: Experimental setup. *(a)* PCM container *(b)* General assembly drawing.

The encapsulated phase change material pretends to tackle the problem of keeping the cold side of the TEG at the proper temperature. Experiments with this material and the obtained results are explained in Section 7.1.

6.2.2 Temperature Gradient Conditions

The TEG is tested at the incidence of solar rays to estimate the actual temperature gradient range during the selected ranges. The testbench for this experiment is presented in Figure 6.11, which consists of a the metal plate on the TEG hot side, and encapsulated PCM on the cold side.

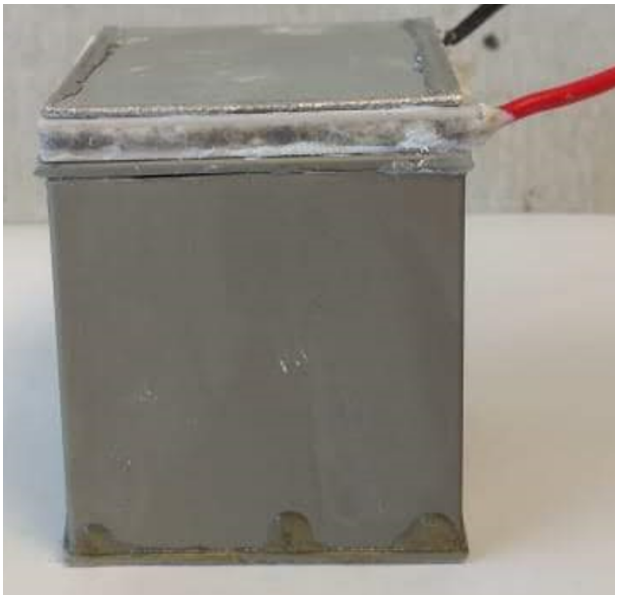

Figure 6.11: Testbench for PCM.

Measurements of TEG cold and hot side are taken each 3 minutes in a span of 5 days. Both temperatures are measured with a K-type thermocouple connected to a microcontroller to store the data during the day and to collect it when the test finishes. A set of 600 data are considered of each variable.

Equation 4.3 allows to estimate the actual temperature gradient experienced by the TEG with the measurements. Then, it is possible to analyze the temperature gradient behavior during the day. Figure 6.12 *(a)* presents the temperature gradient experienced by the TEG during selected ranges. In a general way, the temperature increases during the morning and decreases from 1pm due to internal conduction of the TEG.

Also, the expected output power is calculated using Equation 4.12 with the temperature measurements. The estimation for each day is presented in Figure *(b)*. Considering the temperature gradient profile described in Figure *(a)*, the expected power during the day is higher than 200mW. Comparing those results with the 20% target for solar panels, a minimum power of 268mW should be harvested. It uses the average radiation from Table 2.1.

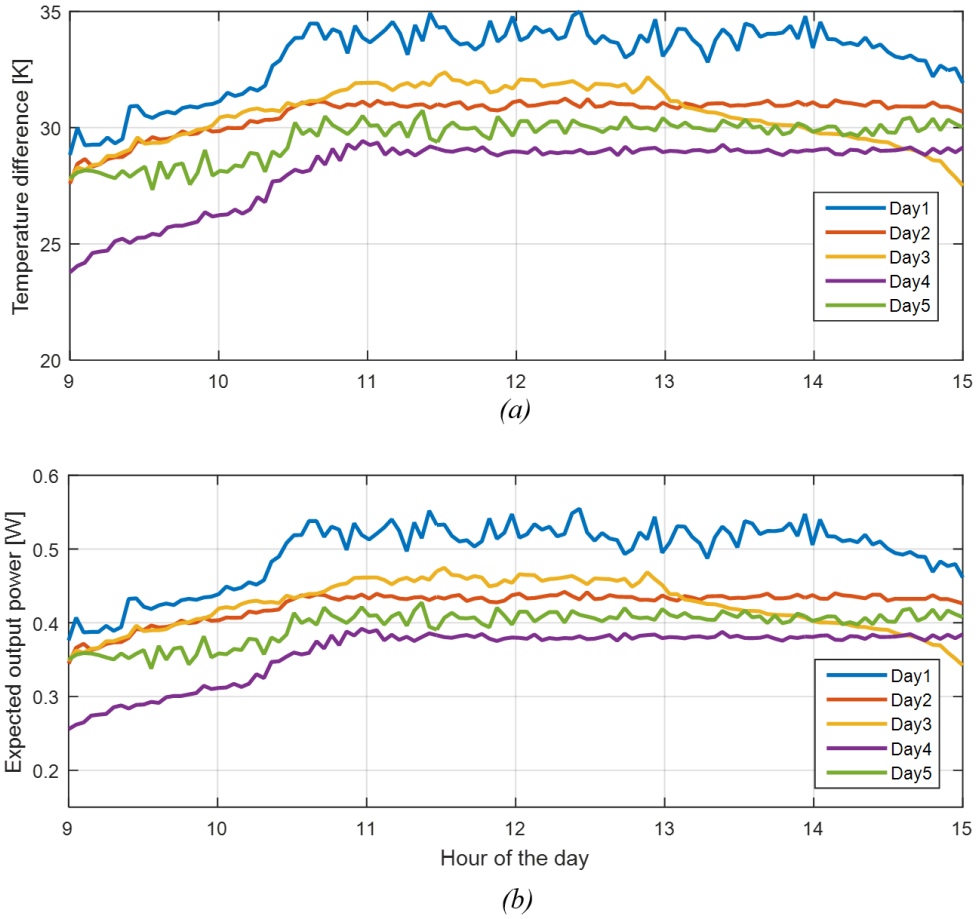

Figure 6.12: Operating conditions for TEG. *(a)* Temperature gradient during the day *(b)* Expected output power.

A statistical analysis of the data is performed. It is found an average temperature gradient of 31.82K with a standard deviation of 1.703K. Confidence intervals of 95% indicate that the true mean temperature gradient is between 31.6113K and 32.0446K for the selected ranges. Also, Table 6.7 presents average temperature gradients, standard deviation and confidence intervals for the mean considering each day. It should be noted that the mean ranges from 29.75K to 33.04K and the standard deviation goes from 0.83K to 1.51K. Confidence intervals indicate that the mean average temperature difference is higher than the 26.31K expected.

Table 6.7: Confidence intervals for mean temperature gradient.

Day	Mean	Stnd. deviation	Lower limit	Upper limit
1	33.04	1.51	32.77	33.31
2	30.61	0.75	30.47	30.74
3	30.57	1.24	30.35	30.79
4	28.17	1.49	27.90	28.44
5	29.75	0.83	29.42	29.72

To calculate the expected energy, the area under the output power curve is approximated using the trapezoid method. Thus, during the six-hour time-frame, the expected average power and energy are listed in Table 6.8.

Table 6.8: TEG expected power and energy.

Day	Average radiation	Average Power	Average Energy
1	890.37 W/m^2	495.2mW	2.9505 Wh
2	751.97 W/m^2	424.3mW	2.5266 Wh
3	783.36 W/m^2	423.8mW	2.5254 Wh
4	594.25 W/m^2	360.3mW	2.1455 Wh
5	682.49 W/m^2	396.1mW	2.3578 Wh

In 3 of the considered days, the average radiation during the day is greater than that shown in Table 2.1 for Ranges V and VI. While the average radiation is slightly lower for the remaining 2 days. It is expected that the days with the highest radiation, have a higher average power and harvested energy. Furthermore, average harvested energy surpasses 2Wh.

6.3 TEG Model Validation

Taking into account the operating conditions described in Section 6.2 and the average ambient temperature of the city of Barranquilla, Colombia; a model validation is proposed for an expected temperature gradient of 31.82K. For this, the electrical model is constructed in LTSpice with the refined parameters. The *V-I* and *P-I* curves are shown in Figure 6.13 *(a)*.

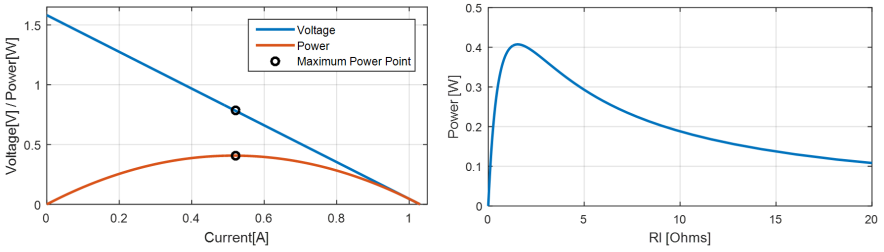

Figure 6.13: TEG curves for the selected operating conditions (simulated data). *(a) I-V* and *P-I* curves *(b) P-*R_L curve.

In addition, the *P-*R_L curve was constructed and presented in Figure 6.13 *(b)*. It shows that for the selected temperature gradient, a MPP of 407.3mW is achieved with an optimum load resistance equal to the series resistance, that is 1.536Ω. This agrees with the maximum power point theorem. Table 6.9 summarizes the theoretical MPP conditions.

Table 6.9: Theoretical MPP conditions.

Parameter	**Value**
$V_{MPP}[V]$	0.7911
$I_{MPP}[A]$	0.5149
$P_{MPP}[W]$	0.4073
$R_L[\Omega]$	1.536

Due to the amount of experiments needed to experimentally validate the model, a stochastic analysis is performed to evidence the changes that would occur in the output power and voltage due to the variation in the internal parameters and operating conditions. The variables considered by the experiment are MPP and voltage at MPP. The Montecarlo simulation used the confidence intervals calculated in Section 6.1.1 and 6.2 for α, R_E and T_H. For this case, 30.000 runs are considered.

6.3.1 Validation of Maximum Power Point

The MPP average and standard deviation of the 30.000 experiments are calculated. An average MPP of 434.834mW with a standard deviation of 45.424mW is found. Thus, for the claim of 20% minimum efficiency, the output power has to be 268.87mW, given the TEG area and the average radiation for Ranges V and VI (see Table 2.1). However, the minimum registered power is 277.734mW for 20.67% efficiency. In addition, statistical validation is performed for a 30% mean efficiency; that is, for a 403.060mW output power. The situation is presented as follows:

- H_0: The mean MPP is equal to or less than 403.060mW.
- H_1: The mean MPP is greater than 403.060mW.

Given the sample mean and standard deviation, the Z statistic is computed and the P-value for the test is found less than 0.05. Then, the null hypothesis is rejected at the 95.0% confidence level. This implies that, with a 95% confidence, the mean output power is more than 403.060mW. In turn, analyzing the confidence intervals for the mean output power, it is obtained that with 95% confidence, this is between 434.32mW and 435.348mW.

6.3.2 Validation of Voltage at Maximum Power Point

In addition, as an input spec for the later sensor power management unit design, the MPP voltage mean and standard deviation of the 30.000 experiments are calculated. A

mean MPP of 816.072mV with a standard deviation of 41.671mV is found. Analyzing the confidence intervals for the mean output voltage, the results are between 815.5mV and 816.543mV, with 95% confidence.

6.4 Prototype Description

Once the TEG is modeled and validated, and the passively-regulated thermal strategy demonstrated, the TEH prototype is designed. The system block diagram consists of one TEG (with the related attached components in both hot and cold sides), a DC-DC converter that provides output ports for a rechargeable battery, and load (see Figure 6.14). The different components are encased in a rectangular package. Given that the TEG and PCM approach has been discussed previously, the complementing blocks are described next.

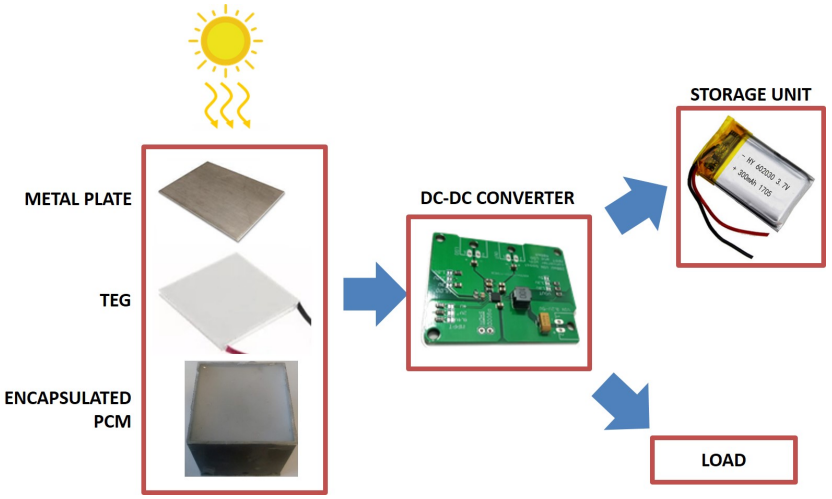

Figure 6.14: Prototype block diagram.

6.4.1 Power Management Unit

Given the TEH available power, a DC-DC converter is included to manage the circuitry and on-board battery. Different energy harvesting converters are evaluated in Table 6.10. To guarantee an overall efficiency over 20%, the key criterion for selecting the converter is the efficiency.

According to the manufacturer, with the operating input voltage (see Table 6.9), the efficiency of ADP5091 does not surpass 80%. As a result, a minimum efficiency of 25% must be fulfilled by the TEG. On the other hand, the efficiency of LTC3105 ranges between 80% and 90% in the selected input voltage. Also, the operating voltage is

Table 6.10: Comparison between different DC-DC converters [115–117].

Converter	Application	Input voltage [V]
ADP5091	Piezoelectric, solar, thermoelectric	80m-3.3
LTC3105	Solar, thermoelectric	200m-5
LTC3108	Thermoelectric	20m-500m

higher than the input voltage for LTC-3108. As a result, an LTC-3105 development board from Linear Technology (Analog Devices) is selected for this purpose (see Figure 6.15 *(a)*). The development board includes a battery charger that regulates the charging process and preserves battery life. Thus, it limits the voltage across the battery to 3.7V, monitors the end-of-charge the minimum battery voltage and avoids the over-discharge.

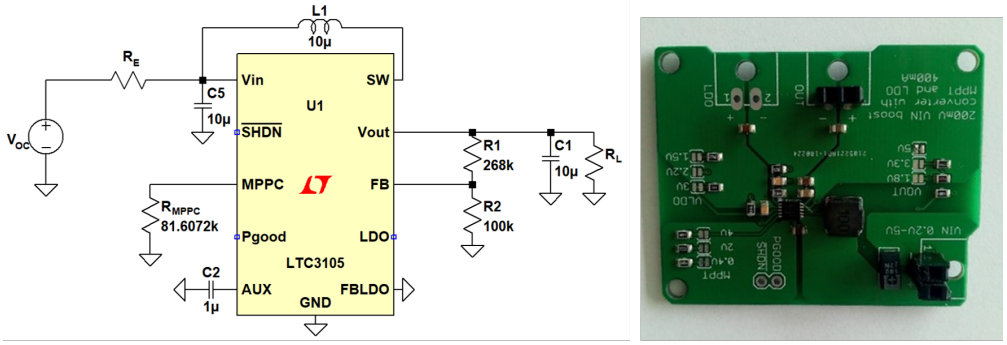

Figure 6.15: LTC3105 DC-DC converter *(a)* Spice model from simulation *(b)* Development board.

The selected board contains a synchronous boost converter that operates from 250mV to 5V. Figure 6.15 *(b)* presents the SPICE model for the validated TEG source, DC-DC converter and a variable load. Using the parameters recommended by the manufacturer [116], a resistor divider is connected between the *VOUT* and *FB* pins to program the step-up converter output voltage as

$$V_{OCV} = 1.004\left(\frac{R_1}{R_2} + 1\right), \tag{6.5}$$

According to Equation 4.11, the MPP voltage is considered half the OCV [118]. Also, it has been validated in Section 6.3.2 that the mean MPP voltage is between 815.5mV and 816.543mV with 95% confidence. With this variation, there is no need to implement an MPPT algorithm, but to use and fix with the TEG mean MPP voltage. Thus, with the information of Section 6.3 about MPP conditions and current suggested by the manufacturer, the MPPT resistor is calculated as

$$R_{MPP} = \frac{V_{MPP}}{10\mu A}. \tag{6.6}$$

The MPPT resistor is connected between *MPPC* and *GND*, as shown in Figure 6.15. Also, a $10\mu F$ decoupling capacitor is connected between V_{in} and *GND*. $\overline{SHDN}$ pin is always open to maintain the converter enabled by an internal pull-up resistor. P_{good} is an open-drain output that indicates when the converter has achieved V_{out}. For this approach, the P_{good} pin is disconnected and *LDO* pin is not used. A 1μF capacitor is connected between *AUX* and *GND*. A 10μF is connected between this pin and *GND* to control the ripple output voltage according to Equation 4.21. Also, an inductor is connected between *SW* and V_{in} according to Equation 4.20.

The transient operation of the DC-DC converter is evaluated via simulation with the MPP load connected to V_{out}. Considering the data delivered by the manufacturer, Figure 6.16 presents a typical start-up sequence. During start-up, the *AUX* output is initially charged. When either V_{in} or *AUX* is greater than 1.4V, the converter enters normal operation until reaching the targeted value of V_{out} meanwhile MPP remains constant.

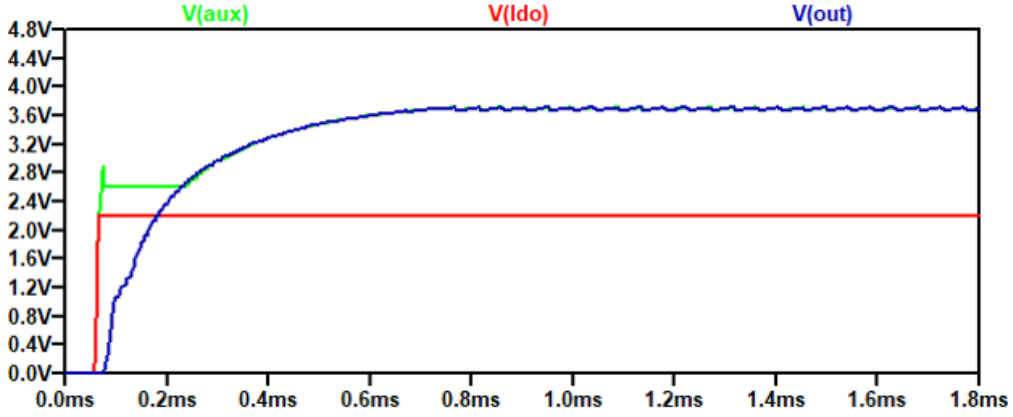

Figure 6.16: LTC3105 DC-DC converter transient response from LTSpice.

The proper operation of the DC-DC converter is also evaluated. For that purpose, load resistances range from 40Ω to 1.5kΩ to ensure that the DC-DC converter can deliver the required power while maintaining the output voltage. It is found that the converter delivers a maximum output power of 420.38mW. Therefore, the efficiency of the DC-DC converter can be calculated as

$$\eta = \frac{P_{OUT}}{P_{IN}} 100\%. \tag{6.7}$$

Using statistical validation from the simulated results obtained for the range of load resistors, the average efficiency is found to be 81.8276% with a standard deviation of 2.98%. Based on the desired results, the situation is presented as follows:

- H_0: The mean efficiency of the DC-DC converter is equal to or less than 80%.
- H_1: The mean efficiency of the DC-DC converter is greater than 80%.

With a P-value of 0.016 the null hypothesis is rejected with 95% confidence. The simulated efficiency mean is between 80.1773% and 83.4779% with 95% confidence.

6.4.2 Load: Case Study of EFM32 microcontroller

As commented in Chapter 2, an remote sensing application requires a low power microcontroller. To make an estimate of the TEH energy budget, theoretical power consumption of a low-power microcontroller is used. Thus, an EFM32 Happy Gecko Evaluation Board (from Silicon Labs) can be evaluated for that purpose. The EFM32 is a 3.3V ultra-low power and easy-to-deploy device that demands a power consumption in both active and sleep modes of 528μW and 1.98μW, respectively. The evaluation board contains an on-chip SI7021 environmental sensor that measures from 233K (-40.15°C) to 358K (84.85°C) temperature and 0% to 80% relative humidity. A RN2483 LoRa transmitter can be used as radio transceiver. Using the parameters reported by the manufacturers, an initial energy budget is constructed and summarized in Table 6.11.

Table 6.11: Energy budget for TEH [119, 120].

Component	**Average Power**	**Duration**	**Consumed energy per day**
Temperature sensor	720μW	20ms	691.2μWh
Humidity sensor	480μW	20ms	460.8μWh
μC (processing)	528μW	3s	76.032μWh
μC (shut-off mode)	66nW	1597s	5.095mWh
Radio transceiver	132mW	150ms	950.4mWh

For this approach, it can be proposed to carry out the environmental variable measurements and sending the data info every 30 minutes. The budget contemplates data reading, processing, sending and microcontroller shut-off mode. Thus, a total energy of 1032.643mWh is needed by the complete unit during the 24-hour time span. In Ranges V and VI, the TEH must be able to power up the system with 258.161mWh and store the remaining energy. Therefore, outside those ranges, a storage system must provide 774.482mWh for continuous operation. Table 6.11 shows that the required peak power is not superior to the peak power that the TEH can provide.

It should be noted that the energy budget presented in Table 6.11 represents a theoretical estimate based on the data delivered by the specs of the development board and radio transceiver.

6.4.3 Energy Storage

Storage units can be employed to complement the operation of TEH when the main source (solar radiation) is not available, such as nighttime. To properly size the required storage unit; first, the expected average power and energy must be considered (see Table 6.8). Then, with the validated internal parameters and the measured temperature gradient from Section 6.2.2, the MPP is calculated using Equation 4.12. Considering the estimated power consumption for the microcontroller, environmental sensor and radio transceiver; secondary batteries and supercapacitors are evaluated as options. Secondary batteries energy densities are one or two orders of magnitude higher than supercapacitors but present higher series resistance. Thus, considering initially a capacitor, the stored energy is defined as

$$W = \frac{1}{2}CV^2, \tag{6.8}$$

then, to maintain a depth of discharge of 50% and to provide the required energy outside Ranges V and VI, the supercapacitor capacity should be twice the required energy, that is 1,936.2Wh (6,970.32J). Since supercapacitor voltages usually vary from 2.2V to 3.3V, then using the maximum voltage, a capacitance of 1,280.1F would be required. As a result, a supercapacitor is not a practical option as storage unit given the energy capacity requirements for the sensor. It is important to note that a 50% DoD is initially considered to have a proper trade-off between energy storage and battery lifetime [121].

Therefore, among secondary batteries, lithium-based batteries are most widely used for portable and space-constrained devices. These present capacities less than 1Ah and operate up to 20 years over a wide temperature range. Thus, for the required 1,936.2Wh, outside Ranges V and VI, a 3.7V 550mAh Li-Po battery meets the required energy specification. Since the battery capacity is 2.035Wh, a first-order approximation indicates that the sensor is operating with a 53.41% DoD, which indicates that the battery lifetime is slightly improved.

6.5 Arrays

It is desired to evaluate the energy density and efficiency of TEG arrays connected thermally in parallel. Different TEG units and types of electrical configuration are theoretical evaluated and simulated. The validated parameters of Section 6.1.1, α and R_E, and the operating conditions from Section 6.2.2, ΔT, are used to model the TEGs.

6.5.1 2-TEG array

Having two TEGs, only two types of electrical configuration can be performed: series and parallel connection (see Figure 6.17).

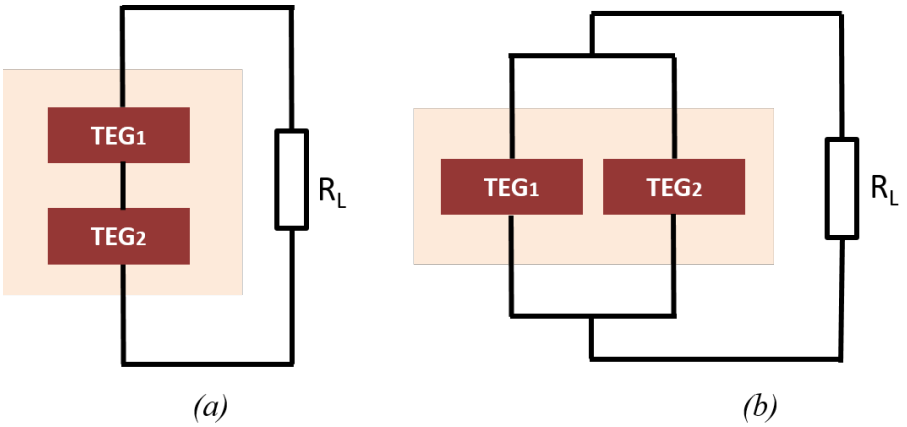

Figure 6.17: 2-TEG array *(a)* Series connection *(b)* Parallel connection.

First, a theoretical analysis is carried out to calculate the OCV and series resistance for the array, and to present an equivalent model according to Figure 4.4. The results are shown in Table 6.12

Table 6.12: 2-TEG theoretical results

Connection	$OCV_{(ARRAY)}$	$R_{E(ARRAY)}$
Series	$2V_{OC}$	$2R_E$
Parallel	V_{OC}	$R_E/2$

It should be noted that V_{OC} and R_E represents the OCV and series resistance of only one TEG. Then, A spice-based simulation is performed in SPICE with fixed internal parameters. The purpose is to evaluate the MPP delivered by the array, MPP voltage, and the efficiency. Table 6.13 presents the simulated results. Average radiation in Ranges V and VI is still taken for the efficiency calculation. Also, the considered area is $32cm^2$.

Table 6.13: 2-TEG simulated results

Connection	**MPP [mW]**	V_{MPP}[V]	$R_{MPP}[\Omega]$	η[%]
Series	0.8146	1.5822	3.072	30.31
Parallel	0.8146	0.7911	0.768	30.31

Assuming that the two TEGs experience the same temperature difference, the total power of both arrays (series and parallel) is equal to twice the power of a single TEG. However, the conditions of V_{MPP} and the series resistance do vary. For the case of a serial connection, V_{MPP} and R_{MPP} are twice the values for one TEG, while for a shunt connection V_{MPP} is equal to that of a single TEG and the series resistance is half R_E. The differences between V_{MPP} and R_{MPP} are due to the equivalent models used for the simulated arrays (see Figure 4.4).

In addition, to be capable of powering a load up, the arrangement must be coupled with the DC-DC converter, but its efficiency also depends on the input voltage. In the case of LTC3105, the efficiency increases according to the input voltage, therefore it is expected that the arrangement with TEG in series has greater overall efficiency. Section 7.4 evaluates the overall efficiency of both arrays via simulation.

6.5.2 3-TEG array

With an array of 3 TEGs, 4 types of connection can be evaluated. Figure 6.18 shows the possible combinations.

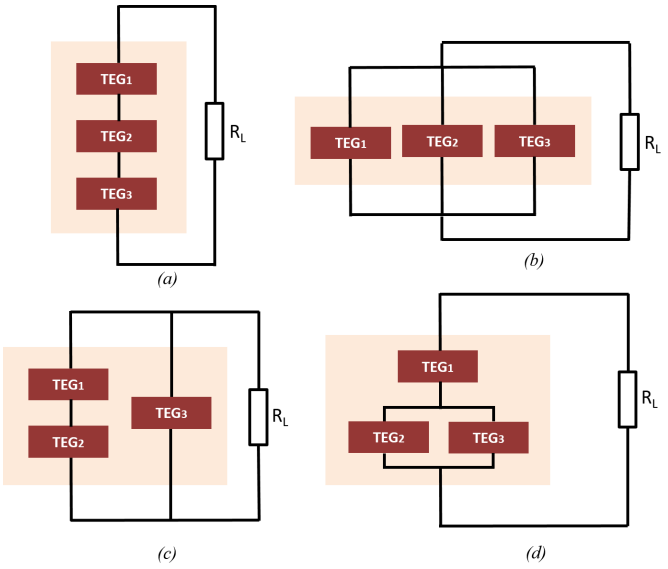

Figure 6.18: 3-TEG array *(a)* Type-1 connection *(b)* Type-2 connection *(c)* Type-3 connection *(d)* Type-4 connection.

Then, a theoretical analysis is carried. This permits to analyze the theoretical behavior of the array with the electrical models from Figure 4.4 and the validated parameters from Section 6.1.1. Using circuit analysis techniques and Thevenin's theorem, OCV and series resistance are obtained for the 4 arrays presented in Figure 6.18. The results are shown in Table 6.14

Table 6.14: 3-TEG theoretical results

Connection	$OCV_{(ARRAY)}$	$R_{E(ARRAY)}$
1	$3V_{OC}$	$3R_E$
2	V_{OC}	$R_E/3$
3	$4V_{OC}/3$	$2R_E/3$
4	$2V_{OC}$	$3R_E/2$

Also, the arrays are simulated using LTSpice. Table 6.15 presents the conditions for the MPP assuming that all are exposed to the same temperature gradient. From the results, Type-1 and Type-2 configurations present the highest conversion efficiency in an area of $48cm^2$.

Table 6.15: 3-TEG simulated results.

Connection	**MPP [W]**	V_{MPP}**[V]**	$R_{MPP}[\Omega]$	η[%]
1	1.22	2.373	4.608	30.27
2	1.22	0.791	0.512	30.27
3	1.08	1.055	1.024	26.79
4	1.08	1.582	2.304	26.79

Although Type-1 and Type-2 have the same generation efficiencies, they have differences in the V_{MPP} and R_{MPP}. This affects the overall efficiency of the other components that must be added to the system. The same situacion is presented in Type-3 and Type-4 arrays. Section 7.4 evaluates the overall efficiency of all arrays via simulation, including the coupling with the DC-DC converter.

6.5.3 4-TEG array

For the analysis of 4-TEG, the 7 configurations evaluated in [122] are selected and presented in Figure 6.19. In addition, the Type-7 configuration is added (see Figure 6.19 *(g)*) for a total of 8 possible combinations. The results of the theoretical analysis for the array are shown in Table 6.14. With those results, the arrays are modeled as a voltage source, $OCV_{(ARRAY)}$, with a series resistance $R_{E(ARRAY)}$. However, the simulation is carried out by coupling equivalent models for each TEG.

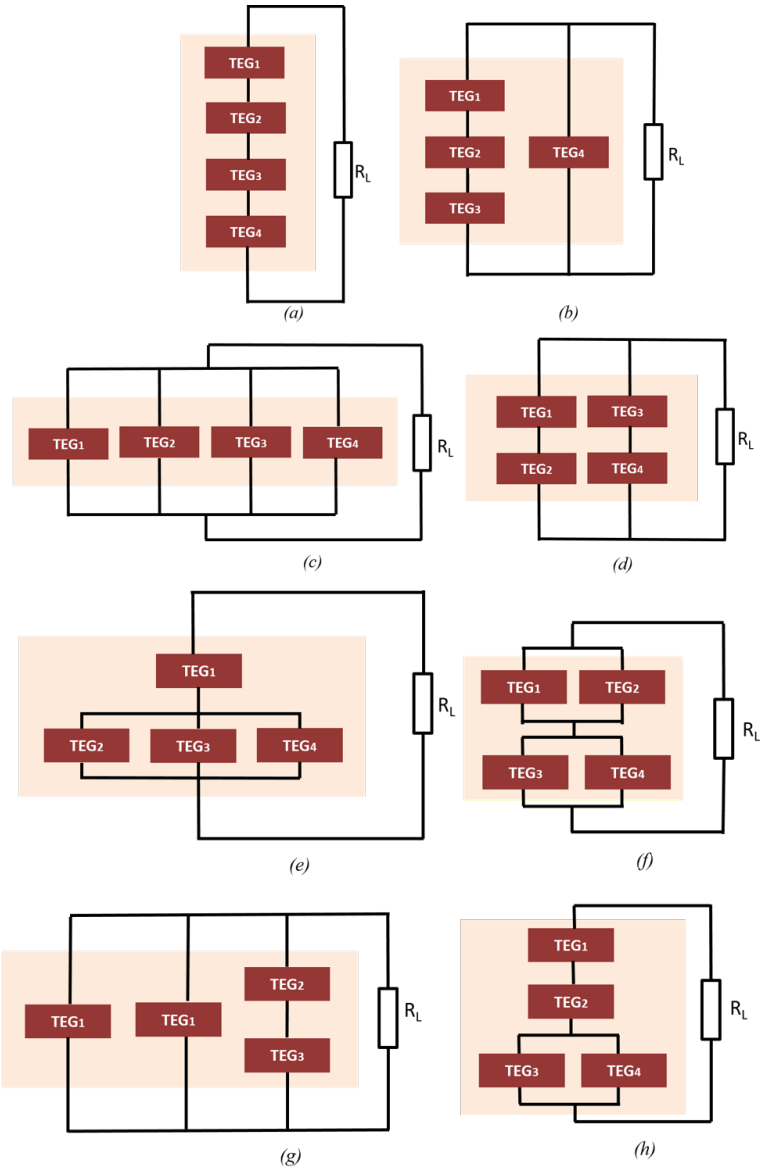

Figure 6.19: 4-TEG array (adapted from [122]) *(a)* Type-1 connection *(b)* Type-2 connection *(c)* Type-3 connection *(d)* Type-4 connection *(e)* Type-5 connection *(f)* Type-6 connection *(g)* Type-7 connection *(h)* Type-8 connection.

Table 6.16: 4-TEG theoretical results

Connection	$OCV_{(ARRAY)}$	$R_{E(ARRAY)}$
1	$4V_{OC}$	$4R_E$
2	$3V_{OC}/2$	$3R_E/4$
3	V_{OC}	$R_E/4$
4	$2V_{OC}$	R_E
5	$2V_{OC}$	$4R_E/3$
6	$2V_{OC}$	R_E
7	$5V_{OC}/4$	$2R_E/5$
8	$3V_{OC}$	$5R_E/2$

The differences with theoretical $OCV_{(ARRAY)}$ and series resistance are due to the electrical models used and how they are affected by the connections of the arrangements. Table 6.17 presents the simulated results in LTSpice for MPP and efficiency of the 8 combinations, assuming a total area of $64cm^2$.

Table 6.17: 4-TEG array results.

Connection	**MPP [W]**	V_{MPP}**[V]**	$R_{MPP}[\Omega]$	η[%]
1	1.629	3.164	6.144	30.31
2	1.222	1.185	1.152	22.70
3	1.629	0.791	0.384	30.31
4	1.629	1.581	1.536	30.31
5	1.222	1.567	2.048	22.70
6	1.629	1.581	1.536	30.31
7	1.466	0.949	0.614	27.27
8	1.466	2.373	1.627	27.27

Type-1, Type-3, Type-4 and Type-6 present less power losses due to the series resistance (see $R_{E(ARRAY)}$ in Table 6.16); and therefore have the highest conversion efficiency. This agrees with the results presented in [122]. Also, for the 20% efficiency target, a minimum MPP should be 1.11W. For all the configurations, the MPP surpasses the target and with all the assumptions, 4-TEG arrays still present higher efficiency conversion than solar panels. The overall efficiency of all arrays including DC-DC converter is evaluated in Section 7.4.

Chapter 7

Experiments and Results

This chapter presents report evaluations for the proposed TEH scheme. First, the temperature gradient of the proposed TEH system is compared with the one evidenced by a TEG with a metal heat sink. Then, the TEG is compared with a photovoltaic solar panel to carry out performance tests of delivered power and efficiency. It includes tests about the behavior of the DC-DC converter with different load resistances. All statistical analyzes are performed using Statgraphics Centurion 18 software.

7.1 Comparison Between Phase Change Material and Metal Heat Sink

Considering the different cooling methods for SP and TEG exposed in [123] and [124], it is proposed to compare the performance of the chosen PCM with a metal heatsink. Thus, a design of experiments is carried out consisting on two TEG exposed to the same heat source (the sun), one of them fitted with a 1.5cm fin metal heatsink while the other with the encapsulated PCM. Figure 7.1 presents the testbench for both TEG.

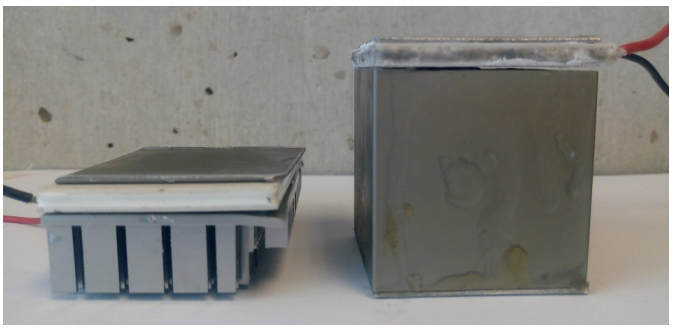

Figure 7.1: Testbench for heatsink (left) and PCM (right).

For this, the temperature in the plates of both TEGs are measured with K-type thermocouples. Then, the temperature difference is calculated using Equation 4.3. The results of the temperature difference in two days are presented in Figure 7.2. As observed; in both experiments, the temperature gradient at the end of the day is higher for the PCM case, which indicates that the system has been thermally regulated with a passive scheme. It is important to note that in situations with radiation over the average, when it is expected to harvest the most energy, the testbench with the heatsink is unable to maintain the temperature gradient as heat transfers from the hot plate to the cold side reducing the electrical output power accordingly. The prototype with heatsink could only be used with solar radiations below the average which is clearly inefficient.

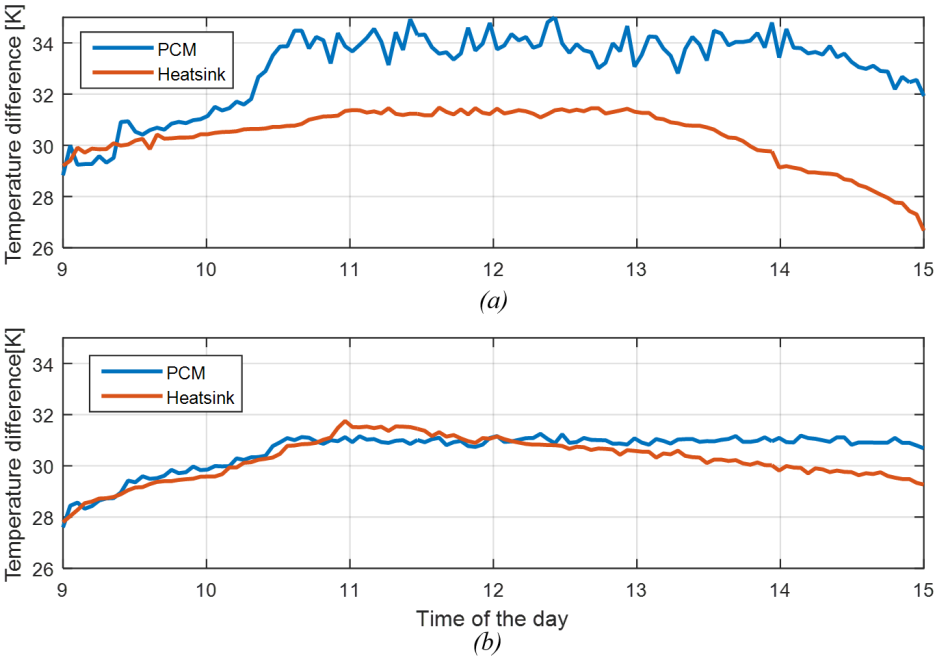

Figure 7.2: Measurements of of ΔT during the day

Using statistical validation from the measurements, the average temperature gradient is found to be 31.827K with a standard deviation of 1.704K for the PCM testbench. On the other hand, the average temperature gradient is found to be 30.31K with a standard deviation of 0.9724K for the heatsink testbench. In addition, hypothesis test is performed for the difference of means for both experiments. The situation is presented as follows:

- H_0: The difference between means μ_{PCM} - $\mu_{heatsink}$ is equal to or less than 1K.
- H_1: The difference between means μ_{PCM} - $\mu_{heatsink}$ is more than 1K.

In the hypothesis test, μ_{PCM} is the true mean ΔT for the PCM testbench and $\mu_{heatsink}$ is the true mean ΔT for the heat sink. Given the sample means and standard deviations, the computed Z statistic equals 3.44502. Since the P-value for the test is less than 0.05, the null hypothesis is rejected at the 95.0% confidence level. The confidence bound shows that the values of the difference between means supported by the data are greater than or equal to 1.32241K. Also, confidence intervals for μ_{PCM} show that the true mean ΔT_{PCM} is between 31.6108K and 32.0443K.

7.2 Comparison Thermoelectric Generator and Solar Panel

As stated, one goal of this work is to propose the use of TEG as a better alternative to solar panels for powering up outdoor sensor and devices. This section focuses in the available power given a defined transducer area, and this metric is defined as efficiency. The purpose is to demonstrate that given the same transducer area, the TEG exhibits higher efficiency than that of a SP within solar radiation Ranges V and VI. It is important to note that to have a fair comparison, dirt and temperature effects in SPs that lower their efficiency are not considered. Figure 7.3 compares dimensions of both devices.

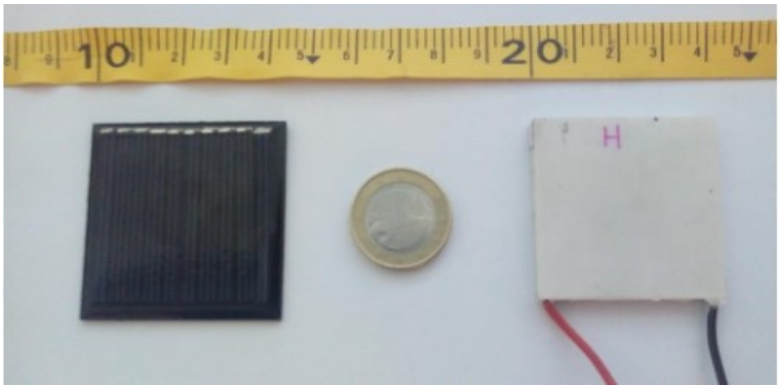

Figure 7.3: Dimension comparison between TEG (left) and PV panel (right).

First, the SP efficiency is calculated from the datasheet specs as

$$\eta = \frac{MPP}{radiation * area}, \tag{7.1}$$

Thus, an efficiency of 5.88% is obtained considering the average solar radiation value for the Range VI (see Table 2.1). Such efficiency value can be explained because the SP found is a low-cost device; however, it serves as reference for the present analysis. In any case, this work also considers a 20% efficiency reference as metric exhibited for good quality SPs.

Notice that the TEG area equals $16cm^2$; then, given the average solar radiation value for the Range VI (see Table 2.1), the maximum output power potential would be 1.34W ($\eta = 100\%$); however, for the 20% efficiency target, the expected power output from the TEG should be at least 268mW. Since the TEG testbench is already set up (metal plate, heat sink and dissipative material), and the range of temperature gradients has been established (Figure 6.12), the efficiency is estimated from temperature, current and voltage measurements using the testbench presented in Figure 6.1 the optimum resistance found in Sections 6.1.1 and 6.1.2. As described, the TEG and the solar panel are exposed to the same energy source, and maintaining the initial temperature of the TEG cold plate is the key for maximization of its power output. Table 7.1 summarizes the efficiency estimates revealing that the performance hypothesis is fulfilled, and the use of a TEG as power supply as better option than SPs is demonstrated.

Table 7.1: TEG efficiency with optimum R_L.

ΔT **[K]**	**Power [mW]**	η [%]
25	242.83	18.12
30	350.18	26.06
35	476.44	35.46
40	623.4	46.4

For temperature differences above 30K, the efficiency exceeds that presented by any commercial solar panel. Although a temperature difference of 40K has an efficiency of 46.4%, it is not possible to obtain those operating conditions with the radiation levels and hot plate temperatures. Even so, if a PCM with lower phase change temperature is used, it melts in contact with the ambient temperature and must be thermally insulated with another mechanism. Those conditions are not considered for this approach.

7.3 Thermoelectric Energy Harvesting Performance Tests

7.3.1 Performance of the DC-DC Converter

This experiment consists of evaluating the performance of the DC-DC converter. That is, the behavior of voltage and power delivered by the circuit for operating conditions shown in Section 6.2.2. Using the arrangement of TEG, PCM and DC-DC converter; and using a 200 Ω potentiometer as load resistance, output voltage and current are measured. The output power is calculated and the results for output voltage and power are presented in Figure 7.4.

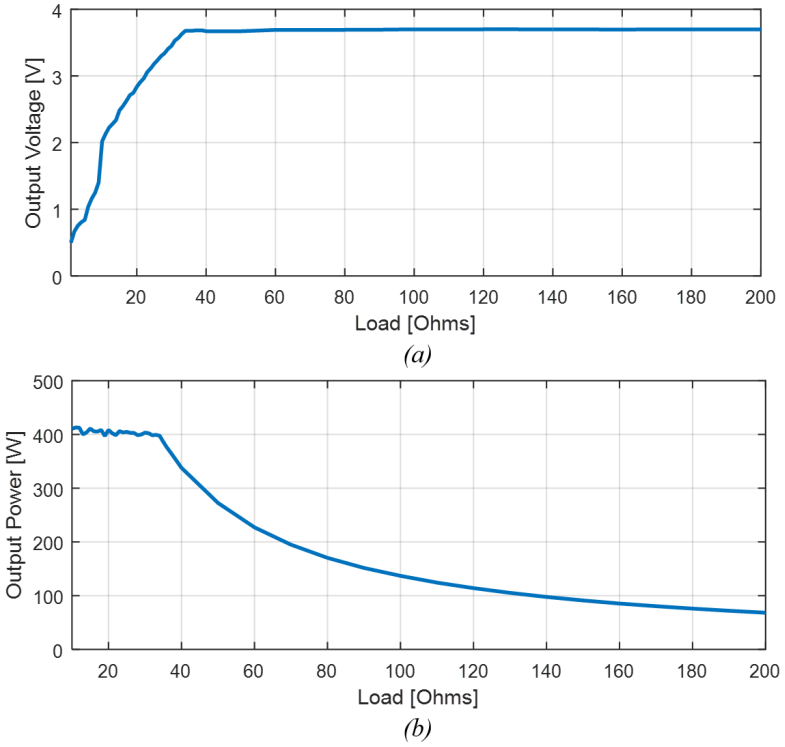

Figure 7.4: Measurements of output voltage and power of DC-DC converter.

From the simulation of Section 6.4.1, the DC-DC converter can provide a maximum power of 420.38mW under the proposed operating conditions. To maintain the output voltage in 3.7V, the minimum connected load must be 32.56Ω. This situation is observed in 7.4 *(a)*. Load resistances below 32.56Ω require more output power than the TEG is capable of transform, resulting in lower output voltages. From 1Ω to 32.56Ω the voltage increases until 3.7V but the power remains constant in 409.11mW. This results in an error percentage of 2.68%. From 32.56Ω, the DC-DC is able to maintain its voltage in 3.7V and delivers the required power to the load.

7.3.2 Performance of the TEH prototype

This design of experiments pretends to evaluate the performance of the complete prototype. First, measurements of radiation are obtained from available data of a local Davis Vantage Pro 2 Personal Weather Station (PWS). The PWS reports every 15 minutes, and solar radiation measurements for 60 days (during March, April and May 2019) are finally gathered. For that particular set of information, the percentiles for the average solar radiation are calculated and summarized in Table 7.2. Assuming a normal distribution, both tails of 10% are used to determine that 5.0% of the mean radiation is below 383.0W/m^2 and 5% of the mean radiation is over 907.357 W/m^2.

Table 7.2: Percentiles for solar radiation.

Percentiles	**Solar radiation** [$\mathbf{W}/m^2$]
1%	196.38
5%	383.0
10%	493.155
25%	592.041
50%	624.341
75%	733.29
90%	811.611
95%	907.357
99%	916.06

First, the devised unit is placed under the influence of solar rays with the battery completely discharged. Figure 7.5 show the power delivered in Ranges V and VI for days using percentiles 5% (three days) and 95% (two days).

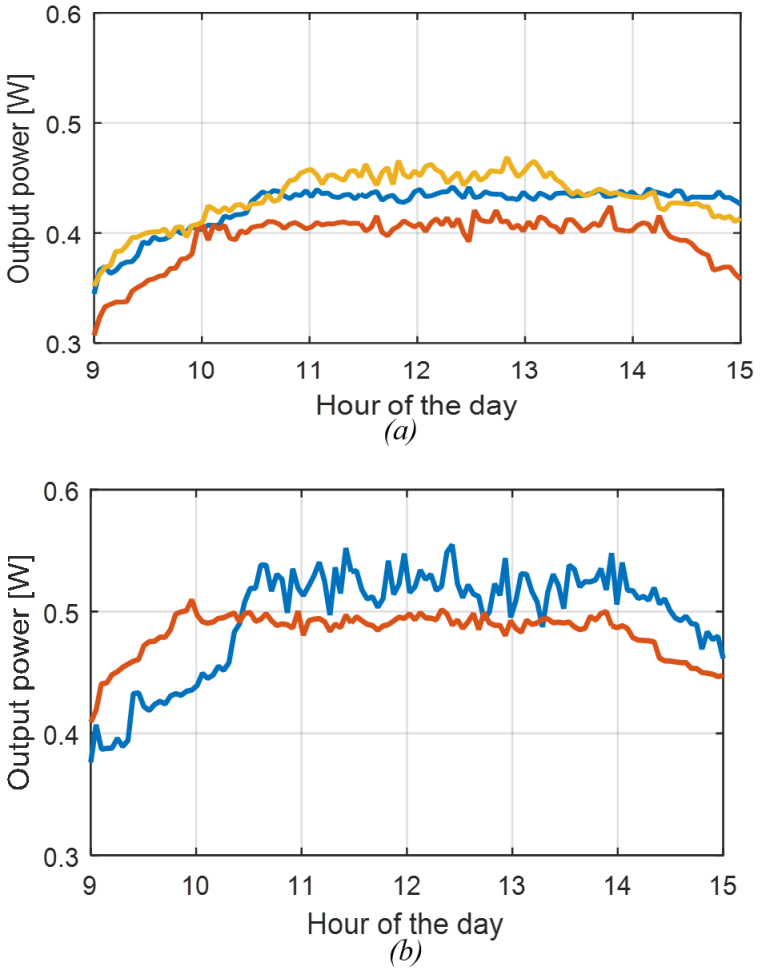

Figure 7.5: Measurements of power delivered by the TEG during selected ranges.

Given the prototype, performance tests are developed to fulfill the following requirements:

- The prototype maintains the efficiency of the arrangement (TEG + DC/DC converter) in at least 20% during Ranges V and VI.
- The prototype is able to power a sensor and charge the on-board battery during the selected radiation ranges.
- The charged battery is able to satisfy the energy demand during the night up to a discharge percentage of 50%.

Using the measurements presented on Figure 7.5, an average output power variation from 335mW to 480mW is obtained. This produces an average efficiency that ranges from 21% to 34.38%. The calculated efficiency takes as incident radiation the one measured for the particular day. In any case, a statistical validation is carried out to determine if the complete prototype maintains the claimed efficiency (over 20%) during the selected ranges; that is, an average output power is greater than 320mW. The situation is presented as follows:

- H_0: The mean output power is equal to or less than 320mW.
- H_1: The mean output power is greater than 320mW.

Considering the proposed hypothesis test, the one-tail model of the standard normal distribution is used to reject the null hypothesis . The right tail of the distribution is taken for a level of significance of α equal to 5% and with it, a $Z = 1.645$. The Z statistic for this type of test is greater than the 0.05 Z-value considered according to the level of significance. Therefore, the null hypothesis is rejected with a 95% certainty. This means that, the average output power is greater than 320mW and the efficiency is maintained over 20% with 95% confidence.

Table 7.3 presents the total energy produced in both types of radiation level considered. As observed, about 2.45Wh is harvested from the TEG for the worst-case scenario; and from the energy budget consideration of Section 6.4.2, the TEH scheme provides enough energy not only to power up the microcontroller, sensors and radio transceiver, but also to charge the battery during the selected ranges. Finally, a maximum power of 132mW is required when the transceiver is sending; and since the TEG average power surpasses that value, the harvester is also capable of maintaining the transceiver powered.

Table 7.3: TEG harvested energy.

Day	Harvested energy
1	2.52 Wh
2	2.95 Wh
3	2.45 Wh
4	2.57 Wh
5	2.87 Wh

From 7.3 and with the statistic validation presented before, harvested energy satisfies the energy demand of the IoT sensor and storage unit during an entire day.

The stochastic behavior of the radiation during the year must be considered to guarantee a continuous operation of the sensor. Black or no-sun days represent the amount of days of the month with radiation levels that are not suitable for electrical generation [13]. Figure 7.6 presents average days during the month with data collected for 30 years from the NASA.

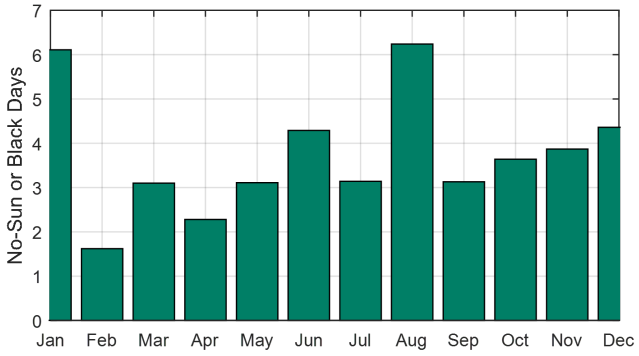

Figure 7.6: Average no-sun days per month (data from [13]).

Average no-sun days vary from 1.79 to 6.23. With the designed DoD, the scheme ensures that, in average, the sensor presents a continuous operation during the month. As a result of all the experiments and radiation patterns delivered by NASA, the potential of TEGs as power source using solar radiation as energy is demonstrated.

7.4 Efficiency of Arrays with DC-DC converter

After analyzing the conversion efficiency in Section 6.5, each one of the arrays (with 2-TEG, 3-TEG and 4-TEG) are simulated in spice-based software with the selected DC-DC converter. Load resistances vary from 50Ω to 1.5kΩ. The results of the simulation are presented in Table 7.4.

Table 7.4: Overall efficiency of arrays.

Number of TEGs	**Connection**	η_{DC-DC}[%]	η_{total}[%]
2	Series	88.95	26.96
	Parallel	84.83	25.71
3	1	85.37	25.84
	2	82.29	24.9
	3	86.55	23.18
	4	89.54	23.98
4	1	-	-
	2	88.97	**19.92**
	3	81.38	24.66
	4	93.23	28.25
	5	91.2	20.70
	6	92.68	28.09
	7	88.67	24.18
	8	84.32	22.58

According to the specifications delivered by the manufacturer, the efficiency of the DC-DC increases until exceeding 90% with the increase of the input voltage. However, at approximately 2.65V, the efficiency decrease considerably [116]. The MPP voltage of Type-1 array surpasses 2.65V; as a result, this configuration is not studied for 4-TEG. The results presented in Table 7.4 for the rest of the arrays show that Type-4, Type-5 and Type-6 with 4-TEG present the highest average DC-DC converter efficiencies.

On the other hand, the overall efficiency is calculated by multiplying the TEG conversion efficiency and the average converter efficiency. The array that presents the highest overall efficiency is 4-TEG in Type-4 configuration, with 28.09%. This configuration presents a TEG maximum power point voltage of 1.567V and the highest DC-DC converter efficiency, that is, 93.23%.

From a general point-of-view, 12 of the 14 arrays studied surpass the 20% efficiency target. As a result, those are demonstrated as better solution than solar panels. Without considering the size of the device, Type-4 TEG is considered the best option to implement. However, if the TEH scheme is required for smaller devices, that is, using only 2 TEGs, the series connection presents the highest overall efficiency in only $32cm^2$. In the case of 3 TEGs, the highest efficiency is presented by connecting all TEG in series, for an area of $48cm^2$, but this is lower than using 2-TEG because of the losses in the DC-DC converter.

Also, only the Type-2 configuration with 4-TEG presents an average efficiency below the 20% target. This is not suitable for TEH scheme considered the stochastic behaviour of solar radiation and average black days presented in Figure 7.6.

Chapter 8

Conclusions and Future Work

This thesis has demonstrated the potential of electric generation using thermoelectric effect under the incidence of solar rays. It has shown a complete energy harvesting system that supports the operation of a secondary battery to power up outdoor devices. The energy harvesting strategy employs the solar resource but increases the conversion efficiency reducing adverse effects such as heating and soiling exhibited by solar panels. Thus, the thermal gradient is preferred over the photovoltaic effect through a comparative analysis. The complete harvesting system complements the TEG selected as transducer with all the required blocks to properly manage battery cycles that maximize lifetime by ensuring a DoD of at most 50%.

Characterizing a TEG is important to determine the associated electric potential and for simulation purposes. Initially, a first-order transducer model has been proposed based on the associated basic electrical parameters. Thus, it is shown that 407.3mW output power and 2.4438Wh energy are obtained using SPICE-based simulations. This helps the design process when simulating the coupling with other electronic components. The key aspect for proper use of thermoelectrical harvesting is maximizing the temperature gradient that experiences a TEG given certain environmental conditions. For the case of this work, the City of Barranquilla counts with large solar resource; therefore, a metal plate is attached to the TEG hot-plate for proper thermal conduction, and a dissipative material is required to keep the initial TEG cold-side temperature as constant as possible. The PCM becomes the ideal choice as dissipative material a phase change at a temperature as close as possible to the ambient. Thus, while the metal plate continues to heat up, the cold side temperature is maintained keeping the targeted temperature gradient and with that the desired efficiency. To verify its advantage for cooling, the PCM is compared to a heatsink. It is found that the PCM reaches an average temperature gradient of 33.1K, while heatsink only gets an average temperature

gradient of 31.05K. This represents an improvement of 2.05K, which corresponds to an average of 106mW more power; which for the selected operating hours represents about 424mWh or an increment of 14.37% in the total harvested energy. Aso, with the temperature gradient measured, the energy density requirements are fulfilled.

It is found that employing the TEG with the passive cooling strategy, the TEH has enough power to operate one low-power microcontroller, sensors and radio, that demand an average energy of 1.032Wh during the day. Also, it is demonstrated that the prototype supplies sufficient energy for continuous operation even during times with no solar resource through an on-board 2.035Wh battery. Such battery can be recharged once the solar radiation is available without compromising the continuous device operation. Corroborating that there is enough energy for sensor autonomy is determined mainly in the case of days with solar radiation below the estimated average for the geographical zone considered. Thus, the designers are considering the worst-case scenario. Power electronics have proved their contribution to adequate power into the proper voltage and current ranges defined by the sensor circuitry. An 80.81% average efficiency DC-DC converter is selected as power management unit.

The author has been able to demonstrate the efficiency claim of solar radiation conversion over SP efficiencies. Statistically, it is found that the efficiency of the prototype surpasses 20% with 95% of confidence in solar-radiation Ranges V and VI. Also, the TEH strategy do not suffer from efficiency reductions due to solar panel heating and/or soiling. It has been shown that with a TEH area of only $16cm^2$, a minimum of 2.45Wh can be easily harvested during a six-hour time span, and such energy level is enough for low-power oriented sensors.

Finally, when evaluating arrays of 2-TEGs, 3-TEGs and 4-TEGs under the same temperature conditions, the efficiency is still maintained over 20%. However, when coupling these arrays with power management units, the efficiency decreases until ranging from 19.92% to 28.25%. When considering the efficiency for arrays, it is necessary to evaluate the required area at the location. For $32cm^2$ it is found a maximum average efficiency of 26.96%, while it is found an efficiency of 25.84% $48cm^2$. In the case of $64cm^2$ the maximum average efficiency is found to be 28.25%.

As future work, it is proposed to perform experimental validation of the behavior of TEG arrays to compare with the simulated results. In addition, it is proposed to make the implementation in a low-power microcontroller and radio transceiver, not only for the case of a single TEG, but for the arrangements considered in this study.

Appendix A

Certificate of Attendance

Obtained results were presented at IEEE Sensors Applications Symposium (SAS) 2019 as an application of **Energy Harvesting for Sensors**. SAS 2019 took place on March 11^{th} to 13^{th} at University of Nice (Sophia Antipolis, France).

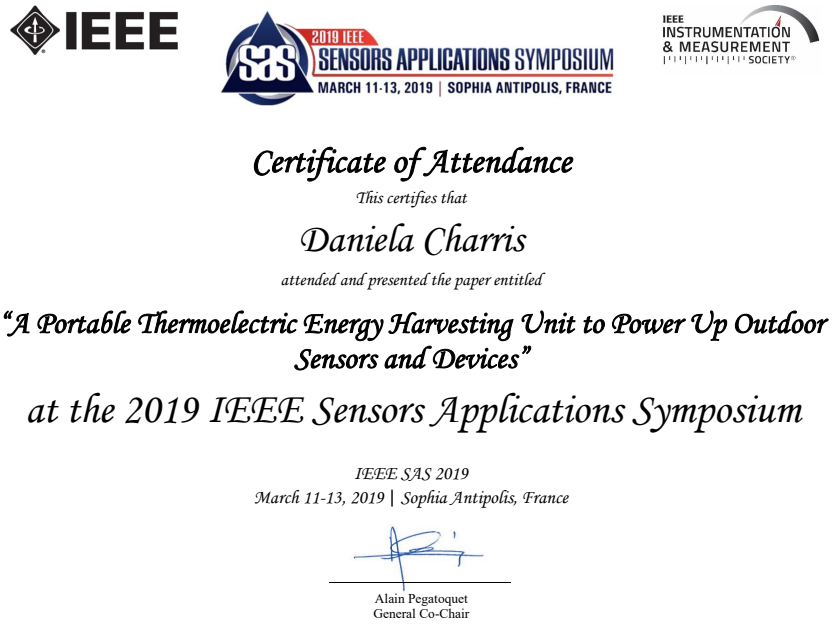

Figure A.1: Certificate of attendance and presentation at international conference.

Appendix B

Student Travel Grant

The paper presented at SAS 2019 was recipient one of the offered student travel grants by fulfilling the following requirements:

- The paper was marked as a student paper.
- The student was the first author
- The student was registered and attended the symposium.
- The paper was of high-quality content and was favorably reviewed by the SAS 2019 Steering Committee.

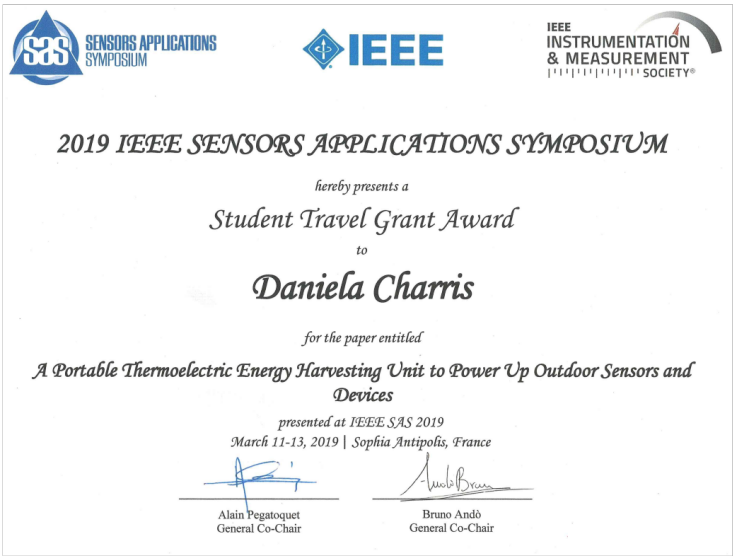

Figure B.1: Certificate of student travel grant.

Bibliography

[1] E. Ismagilova, L. Hughes, Y. K. Dwivedi, and K. R. Raman. Smart cities : Advances in research — An information systems perspective. *International Journal of Information Management*, 47(December 2018):88–100, 2019.

[2] M. Rungger and P. Tabuada. A notion of robustness for cyber-physical systems. *IEEE Transactions on Automatic Control*, 61(8):2108–2123, Aug 2016.

[3] Jose-Miguel Horcas, Mónica Pinto, and Lidia Fuentes. Context-aware energy-efficient applications for cyber-physical systems. *Ad Hoc Networks*, 82:15 – 30, 2019.

[4] T. Sanislav, S. Zeadally, G. D. Mois, and S. C. Folea. Wireless energy harvesting: Empirical results and practical considerations for Internet of Things. *Journal of Network and Computer Applications*, 121(June):149–158, 2018.

[5] P. Choudhary and R. K. Srivastava. Sustainability perspectives- a review for solar photovoltaic trends and growth opportunities. *Journal of Cleaner Production*, 227:589 – 612, 2019.

[6] M. A. Green, Y. Hishikawa, E. D. Dunlop, D. H. Levi, J. Hohl-Ebinger, M. Yoshita, and A. Ho-Baillie W.Y. Solar cell efficiency tables (Version 53). *Progress in Photovoltaics: Research and Applications*, 27(1):3–12, 2019.

[7] F. Deng, H. Qiu, J. Chen, L. Wang, and B. Wang. Wearable thermoelectric power generators combined with flexible supercapacitor for low-power human diagnosis devices. *IEEE Transactions on Industrial Electronics*, 64(2):1477–1485, Feb 2017.

[8] D. Champier. Thermoelectric generators: A review of applications. *Energy Conversion and Management*, 140:167–181, 2017.

[9] L. Kutt, J. Millar, A. Karttunen, M. Lehtonen, and M. Karppinen. Thermoelectric applications for energy harvesting in domestic applications and micro-production units. Part I: Thermoelectric concepts, domestic boilers and biomass stoves. *Renewable and Sustainable Energy Reviews*, 98(December 2015):519–544, 2018.

[10] W. He, G. Zhang, X. Zhang, J. Ji, G. Li, and X. Zhao. Recent development and application of thermoelectric generator and cooler. *Applied Energy*, 143:1–25, 2015.

[11] Instituto de Hidrología Meteorología y Estudios Ambientales. Atlas de radiación solar ultravioleta y ozono de colombia, 2009.

[12] K. Bakirci. Models of solar radiation with hours of bright sunshine: A review. *Renewable and Sustainable Energy Reviews*, 13(9):2580 – 2588, 2009.

[13] *NASA Surface Meteorology and Solar Energy.* Atmospheric Science Data Center, Mar 2017.

[14] U. Meier. A note on the power of fisher's least significant difference procedure. *Pharmaceutical statistics*, 5:253–63, 10 2006.

[15] *Solar Catalogue.* Sollatek Solar Systems, June 2010. Harnessing the power of the sun.

[16] *Product catalogue 2014.* Tritec, Dec 2014. Energy for a better world.

[17] *2018 Solar Catalogue.* Proinso: Proffesionals in solar, Mar 2018. Your one-stop-shop for integrated PV solutions.

[18] *Solar Power: Product Catalogue 2015.* Yhi Power, Oct 2015.

[19] *Solar Module's Catalog.* ModulTeq: Technik für Solarenergie, Jan 2011. Veredeln Sie Sonnenergies in bares geld.

[20] B. Abhilash and A. K. Panchal. Self-cleaning and tracking solar photovoltaic panel for improving efficiency. In *2016 2nd International Conference on Advances in Electrical, Electronics, Information, Communication and Bio-Informatics (AEEICB)*, pages 1–4, Feb 2016.

[21] B. Sreewirote, A. Noppakant, and C. Pothisarn. Increasing efficiency of an electricity production system from solar energy with a method of reducing solar panel temperature. In *2017 International Conference on Applied System Innovation (ICASI)*, pages 1308–1311, May 2017.

[22] J. B. Jawale, V. K. Karra, B. P. Patil, P. Singh, S. Singh, and S. Atre. Solar panel cleaning bot for enhancement of efficiency — an innovative approach. In *2016 3rd International Conference on Devices, Circuits and Systems (ICDCS)*, pages 103–108, March 2016.

[23] M. Kuo and W. Lo. A combination of concentrator photovoltaics and water cooling system to improve solar energy utilization. *IEEE Transactions on Industry Applications*, 50(4): 2818–2827, July 2014.

[24] R. Arshad, S. Tariq, M. U. Niaz, and M. Jamil. Improvement in solar panel efficiency using solar concentration by simple mirrors and by cooling. In *2014 International Conference on Robotics and Emerging Allied Technologies in Engineering (iCREATE)*, pages 292–295, April 2014.

[25] Changcun Li, Fengxing Jiang, Congcong Liu, Peipei Liu, and Jingkun Xu. Present and future thermoelectric materials toward wearable energy harvesting. *Applied Materials Today*, 15:543 – 557, 2019.

[26] W. Xie, G. Huang, X. Zhang, and F. Deng. A maximum power point tracking controller for thermoelectric generators. In *2017 36th Chinese Control Conference (CCC)*, pages 9079–9084, July 2017.

[27] A.R. Dehghani-Sanij, E. Tharumalingam, M.B. Dusseault, and R. Fraser. Study of energy storage systems and environmental challenges of batteries. *Renewable and Sustainable Energy Reviews*, 104:192 – 208, 2019.

[28] F. M. Al-Turjman, H. S. Hassanein, and M. Ibnkahla. Towards prolonged lifetime for deployed wsns in outdoor environment monitoring. *Ad Hoc Networks*, 24:172 – 185, 2015.

[29] E. Sarasketa-Zabala, E. Martinez-Laserna, M. Berecibar, I. Gandiaga, L.M. Rodriguez-Martinez, and I. Villarreal. Realistic lifetime prediction approach for li-ion batteries. *Applied Energy*, 162:839 – 852, 2016.

[30] S. A. R. Zaidi, A. Afzal, M. Hafeez, D. McLernon, M. Ghogho, and A. Swami. Solar energy empowered cognitive metro cellular networks. *IEEE Communications Magazine*, 53, 07 2015.

[31] B. Dziadak, L. Makowski, and A. Michalski. Survey of energy harvesting systems for wireless sensor networks in environmental monitoring. *Metrology and Measurement Systems*, 23, 03 2016.

[32] S. Kamruzzaman, X. Fernando, and M. Jaseemuddin. Energy harvesting wireless sensors for smart cities. pages 218–222, 07 2017.

[33] M. G. Deceglie, L. Micheli, and M. Muller. Quantifying soiling loss directly from pv yield. *IEEE Journal of Photovoltaics*, 8(2):547–551, March 2018.

[34] A. Xenophontos and A. M. Bazzi. Model-based maximum power curves of solar photovoltaic panels under partial shading conditions. *IEEE Journal of Photovoltaics*, 8(1): 233–238, Jan 2018.

[35] N. Sasidharan, W. Ongsakul, M. P. Varghese, V. S. Anooja, and R. Akhila. Efficient improvement of solar photo voitaic system using artificial cooling methods. In *2018 International Conference on Power, Signals, Control and Computation (EPSCICON)*, pages 1–6, Jan 2018.

[36] M. T. Penella-López and M. Gasulla-Forner. *Powering autonomous sensors: An integral approach with focus on Solar and RF Energy Harvesting.* Springer, Springer Dordrecht Heidelberg London New York, 12 2010.

[37] B. Martinez, M. Montón, I. Vilajosana, and J. D. Prades. The power of models: Modeling power consumption for iot devices. *IEEE Sensors Journal*, 15(10):5777–5789, Oct 2015.

[38] O.H. Ando Junior, A.L.O. Maran, and N.C. Henao. A review of the development and applications of thermoelectric microgenerators for energy harvesting. *Renewable and Sustainable Energy Reviews*, 91:376 – 393, 2018.

[39] M.A. Alghoul, S.A. Shahahmadi, B. Yeganeh, N. Asim, A.M. Elbreki, K. Sopian, S.K. Tiong, and N. Amin. A review of thermoelectric power generation systems: Roles of existing test rigs/ prototypes and their associated cooling units on output performance. *Energy Conversion and Management*, 174:138 – 156, 2018.

[40] Y. Hong, S. N. Pham, T. Yoo, K. Chae, K. Baek, and Y. S. Kim. Efficient maximum power point tracking for a distributed pv system under rapidly changing environmental conditions. *IEEE Transactions on Power Electronics*, 30(8):4209–4218, Aug 2015.

[41] P. Luo, D. Peng, Y. Wang, and X. Zheng. Review of Solar Energy Harvesting for IoT Applications. *2018 IEEE Asia Pacific Conference on Circuits and Systems, APCCAS 2018*, pages 512–515, 2019.

[42] T. J. Kaźmierski and S. Beeby. *Energy Harvesting Systems: Principles, modeling and applications*. Springer Science and Business Media, 2010.

[43] H. Xie, Z. Huang, S. Guo, and E. Torru. Feasibility of an electrostatic energy harvesting device for cfcs aircraft. *Procedia Engineering*, 99:1213 – 1222, 2015. 2014 Asia-Pacific International Symposium on Aerospace Technology, APISAT2014 September 24-26, 2014 Shanghai, China.

[44] C. Bao, Y. Dai, P. Wang, and G. Tang. A piezoelectric energy harvesting scheme based on stall flutter of airfoil section. *European Journal of Mechanics - B/Fluids*, 75:119 – 132, 2019.

[45] L. Dal Bo and P. Gardonio. Energy harvesting with electromagnetic and piezoelectric seismic transducers: Unified theory and experimental validation. *Journal of Sound and Vibration*, 433:385 – 424, 2018.

[46] L.B. Kong, T. Li, H. H. Hng, F. Boey, T. Zhang, and S. Li. *Waste Energy Harvesting*. Springer, Berlin, Heidelberg, 03 2014.

[47] M. Cansiz, D. Altinel, and G. K. Kurt. Efficiency in rf energy harvesting systems: A comprehensive review. *Energy*, 174:292 – 309, 2019.

[48] L. Catacuzzeno, F. Orfei, A. Di Michele, L. Sforna, F. Franciolini, and L. Gammaitoni. Energy harvesting from a bio cell. *Nano Energy*, 56:823 – 827, 2019.

[49] M. T. Penella-López and M. Gasulla-Forner. *Powering autonomous sensors: An integral approach with focus on Solar and RF Energy Harvesting*. Springer, Springer Dordrecht Heidelberg London New York, 12 2010.

[50] M. Tomita, S. Oba, Y. Himeda, R. Yamato, K. Shima, T. Kumada, M. Xu, H. Takezawa, K. Mesaki, K. Tsuda, S. Hashimoto, T. Zhan, H. Zhang, Y. Kamakura, Y. Suzuki, H. Inokawa, H. Ikeda, T. Matsukawa, T. Matsuki, and T. Watanabe. Modeling, simulation, fabrication, and characterization of a 10-μw/cm2class si-nanowire thermoelectric generator for iot applications. *IEEE Transactions on Electron Devices*, 65(11):5180–5188, Nov 2018.

[51] X. Zhang and L.D. Zhao. Thermoelectric materials: Energy conversion between heat and electricity. *Journal of Materiomics*, 1(2):92 – 105, 2015.

[52] S. Siouane, S. Jovanović, and P. Poure. Influence of contact thermal resistances on the open circuit voltage mppt method for thermoelectric generators. pages 1–6, April 2016.

[53] S. D. Senturia. *Microsystem Design*. Springer US, 2001.

[54] E. F. Sawires, M. I. Eladawy, Y. I. Ismail, and H. Abdelhamid. Thermal resistance model for standard cmos thermoelectric generator. *IEEE Access*, 6:8123–8132, 2018.

[55] A. Paraskevas and E. Koutroulis. A simple maximum power point tracker for thermoelectric generators. *Energy Conversion and Management*, 108:355 – 365, 2016.

[56] M. Al-Maghalseh and K. Mahkamov. Methods of heat transfer intensification in pcm thermal storage systems: Review paper. *Renewable and Sustainable Energy Reviews*, 92: 62 – 94, 2018.

[57] P. Sivasamy, A. Devaraju, and S. Harikrishnan. Review on heat transfer enhancement of phase change materials (pcms). *Materials Today: Proceedings*, 5(6, Part 2):14423 – 14431, 2018. International Conference on Advanced Functional Materials 2017 (ICAFM'17), 03.05.2017 – 05.05.2017.

[58] A. Gil, M. Medrano, I. Martorell, A. Lázaro, P. Dolado, B. Zalba, and L. F. Cabeza. State of the art on high temperature thermal energy storage for power generation. part 1—concepts, materials and modellization. *Renewable and Sustainable Energy Reviews*, 14 (1):31 – 55, 2010.

[59] G. Boyle. *Renewable Energy*. Oxford University Press, The Open University, Walton Hall, Milton Keynes MK7 6AA, 2 edition, 2004.

[60] M. Green. *Solar Cells: Operating Principles, Technology and System Applications*. Prentice-Hall, Englewood Cliffs, NJ, Prentice-Hall, Inc., 1982. 288 p., 01 1982.

[61] E. I. Batzelis. Simple pv performance equations theoretically well founded on the single-diode model. *IEEE Journal of Photovoltaics*, 7(5):1400–1409, Sep. 2017.

[62] Darwin Cardozo. Modelado y simulación de un sistema de control para un módulo de energía solar fotovoltáica en conexión isla, 2018.

[63] W. Xiao, W. G. Dunford, and A. Capel. A novel modeling method for photovoltaic cells. In *2004 IEEE 35th Annual Power Electronics Specialists Conference (IEEE Cat. No.04CH37551)*, volume 3, pages 1950–1956 Vol.3, June 2004.

[64] M.A. Hasan and S.K. Parida. An overview of solar photovoltaic panel modeling based on analytical and experimental viewpoint. *Renewable and Sustainable Energy Reviews*, 60:75 – 83, 2016.

[65] M. R. Maghami, H. Hizam, C. Gomes, M. A. Radzi, M. I. Rezadad, and S. Hajighorbani. Power loss due to soiling on solar panel: A review. *Renewable and Sustainable Energy Reviews*, 59:1307 – 1316, 2016.

[66] H. Mamur and R. Ahiska. Application of a DC-DC boost converter with maximum power point tracking for low power thermoelectric generators. *Energy Conversion and Management*, 97:265–272, 2015.

[67] D. Hart. *Introduction to Power Electronics*. Prentice Hall, Upper Saddle River, NJ 07458, 1997.

[68] D. Hart. *Power Electronics*. McGRaw-Hill, Avenue of the Americas, New York, NY 10020, 2011.

[69] S. Sivanagaraju. *Power Electronics*. PHI Learning Pvt. Ltd., 2010.

[70] A.W. Cristri and R.F. Iskandar. Analysis and design of dynamic buck converter with change in value of load impedance. *Procedia Engineering*, 170:398 – 403, 2017. Engineering Physics International Conference 2016 – EPIC 2016.

[71] S. Sinha, , A. Gullapalli, S. S. John, and S. Kundu. Dc dc boost converter for thermoelectric energy harvesting. In *2018 International Conference on Current Trends towards Converging Technologies (ICCTCT)*, pages 1–4, March 2018.

[72] H. Yu, M. Chen, C. Wu, K. Tang, and G. Wang. A batteryless and single-inductor dc-dc boost converter for thermoelectric energy harvesting application with 190mv cold-start voltage. In *2018 IEEE International Symposium on Circuits and Systems (ISCAS)*, pages 1–4, May 2018.

[73] A. R. M. Siddique, S. Mahmud, and B. V. Heyst. A review of the state of the science on wearable thermoelectric power generators (TEGs) and their existing challenges. *Renewable and Sustainable Energy Reviews*, 73(December 2016):730–744, 2017.

[74] R. Sharma and. Survey on hybrid (wind/solar) renewable energy system and associated control issues. In *2014 IEEE 6th India International Conference on Power Electronics (IICPE)*, pages 1–6, Dec 2014.

[75] N. Karami, N. Moubayed, and R. Outbib. General review and classification of different MPPT Techniques. *Renewable and Sustainable Energy Reviews*, 68(July 2016):1–18, 2017.

[76] D. Jeong, J. Ko, J. Lee, and D. Chung. Mppt control of photovoltaic system using optimization voltage with temperature. In *2012 12th International Conference on Control, Automation and Systems*, pages 1139–1143, Oct 2012.

[77] Y. Huang, F. Z. Peng, J. Wang, and D. Yoos. Survey of the power conditioning system for pv power generation. In *2006 37th IEEE Power Electronics Specialists Conference*, pages 1–6, June 2006.

[78] A. F. Mirza, Q. Ling, M. Y. Javed, and M. Mansoor. Novel MPPT techniques for photovoltaic systems under uniform irradiance and Partial shading. *Solar Energy*, 184(January): 628–648, 2019.

[79] M. Balato, L. Costanzo, A. Lo Schiavo, and M. Vitelli. Optimization of both Perturb & Observe and Open Circuit Voltage MPPT Techniques for Resonant Piezoelectric Vibration Harvesters feeding bridge rectifiers. *Sensors and Actuators, A: Physical*, 278:85–97, 2018.

[80] T. Kousksou, P. Bruel, A. Jamil, T. El Rhafiki, and Y. Zeraouli. Energy storage: Applications and challenges. *Solar Energy Materials and Solar Cells*, 120:59 – 80, 2014.

[81] R. Dell, D. A. J. Rand, and Jr. R. Bailey. *Understanding batteries*. Royal Society of Chemistry, 01 2001.

[82] F. I. Simjee and P. H. Chou. Efficient charging of supercapacitors for extended lifetime of wireless sensor nodes. *IEEE Transactions on Power Electronics*, 23(3):1526–1536, May 2008.

[83] C. Vankecke, L. Assouère, A. Wang, P. Durand-Estèbe, F. Caignet, J. Dilhac, and M. Bafleur. Multisource and battery-free energy harvesting architecture for aeronautics applications. *IEEE Transactions on Power Electronics*, 30(6):3215–3227, June 2015.

[84] R. Drummond, S. Zhao, D.A. Howey, and S.R. Duncan. Circuit synthesis of electrochemical supercapacitor models. *Journal of Energy Storage*, 10:48 – 55, 2017.

[85] A. Bonci, A. Carbonari, A. Cucchiarelli, L.o Messi, M. Pirani, and M. Vaccarini. A cyber-physical system approach for building efficiency monitoring. *Automation in Construction*, 102:68 – 85, 2019.

[86] J. Yan, X. Liao, D. Yan, and Y. Chen. Review of micro thermoelectric generator. *Journal of Microelectromechanical Systems*, 27(1):1–18, Feb 2018.

[87] L. Hou and S. Tan. A preliminary study of thermal energy harvesting for industrial wireless sensor networks. In *2016 10th International Conference on Sensing Technology (ICST)*, pages 1–5, Nov 2016.

[88] M. Guan, K. Wang, D. Xu, and W. H. Liao. Design and experimental investigation of a low-voltage thermoelectric energy harvesting system for wireless sensor nodes. *Energy Conversion and Management*, 138:30–37, 2017.

[89] H. U. Zaman, C. E. Shourov, A. Al Mahmood, and N. E. A. Siddique. Conversion of wasted heat energy into electrical energy using teg. In *2017 IEEE 7th Annual Computing and Communication Workshop and Conference (CCWC)*, pages 1–5, Jan 2017.

[90] A. Prijić, L. Vračar, D. Vučković, D. Milić, and Z. Prijić. Thermal energy harvesting wireless sensor node in aluminum core pcb technology. *IEEE Sensors Journal*, 15(1): 337–345, Jan 2015.

[91] M. Yun, E. Ustun, P. Nadeau, and A. Chandrakasan. Thermal energy harvesting for self-powered smart home sensors. In *2016 IEEE MIT Undergraduate Research Technology Conference (URTC)*, pages 1–4, Nov 2016.

[92] G Verma and V Sharma. A Novel Thermoelectric Energy Harvester for Wireless Sensor Network Application. *IEEE Transactions on Industrial Electronics*, 66(5):3530–3538, may 2019.

[93] F. Lebahn and H. Ewald. Using atmospheric temperature variations for thermal energy harvesting for wireless sensors. In *2015 9th International Conference on Sensing Technology (ICST)*, pages 133–137, Dec 2015.

[94] S. A. Tahami, M. Gholikhani, R. Nasouri, S. Dessouky, and A.T. Papagiannakis. Developing a new thermoelectric approach for energy harvesting from asphalt pavements. *Applied Energy*, 238:786 – 795, 2019.

[95] W. Jiang, D. Yuan, S. Xu, H. Hu, J. Xiao, A. Sha, and Y. Huang. Energy harvesting from asphalt pavement using thermoelectric technology. *Applied Energy*, 205(August):941–950, 2017.

[96] M. Gao, C. Su, J. Cong, F. Yang, Y. Wang, and P. Wang. Harvesting thermoelectric energy from railway track. *Energy*, 180:315 – 329, 2019.

[97] J. Singh, P. Kuchroo, H. Bhatia, and E. Sidhu. Floating teg based solar energy harvesting system. In *2016 International Conference on Automatic Control and Dynamic Optimization Techniques (ICACDOT)*, pages 763–766, Sep. 2016.

[98] P. C. Dias, F. José, O. Morais, M. Bernadete, D. M. Francca, E. C. Ferreira, and A. Cabot. Autonomous Multisensor System Powered by a Solar Thermoelectric Energy Harvester With Ultralow-Power Management Circuit. 64(11):2918–2925, 2015.

[99] S. A. Atouei, A. Rezania, A. A. Ranjbar, and L. A. Rosendahl. Protection and thermal management of thermoelectric generator system using phase change materials: An experimental investigation. *Energy*, 156:311–318, 2018.

[100] M. Jaworski, M. Bednarczyk, and M. Czachor. Experimental investigation of thermoelectric generator (TEG) with PCM module. *Applied Thermal Engineering*, 96:527–533, 2016.

[101] S. A. Atouei, A. Rezania, A. A. Ranjbar, and L. A. Rosendahl. Protection and thermal management of thermoelectric generator system using phase change materials: An experimental investigation. *Energy*, 156:311–318, 2018.

[102] K. Yoon, S. Hong, J. Bang, S. Lee, S. Choi, and G. Cho. A 1452-simultaneous energy extraction from a piezoelectric transducer and a thermoelectric generator. In *2017 Symposium on VLSI Circuits*, pages C202–C203, June 2017.

[103] J. Zhang and Y. Xuan. An integrated design of the photovoltaic-thermoelectric hybrid system. *Solar Energy*, 177(November 2018):293–298, 2019.

[104] M. Singh, J. Singh, , P. Kuchroo, H. Bhatia, S. Bhagat, G. Sharma, and E. Sidhu. Efficient autonomous solar panel and thermo-electric generator (teg) integrated hybrid energy harvesting system. In *2016 Progress in Electromagnetic Research Symposium (PIERS)*, pages 1764–1768, Aug 2016.

[105] *Thermoelectric Power Generation Tablets*. Elecfreaks, March 2011. Thermoelectric power generation introduction.

[106] *Specification of Thermoelectric Module*. Thermonamic Electronics, Aug 2015. High Performance and Highly Reliable Solution for Cooling and Heating Application.

[107] *Specification of Small Power Solar Cells.* Solarshining Co. Ltd, Apr 2014. Small Power Solar Panel 2V 50mA 45*45*3mm.

[108] *Specification of Small Power Solar Cells.* Solarshining Co. Ltd, Oct 2015. Small Power Solar Panel 5V 160mA 80*80*3.2mm.

[109] T.R. Ayodele, A.S.O. Ogunjuyigbe, and E.E. Ekoh. Evaluation of numerical algorithms used in extracting the parameters of a single-diode photovoltaic model. *Sustainable Energy Technologies and Assessments*, 13:51 – 59, 2016.

[110] Trishan Esram. Modeling and control of an alternating-current photovoltaic module, 2010.

[111] N. Yildiran and E. Tacer. Identification of photovoltaic cell single diode discrete model parameters based on datasheet values. *Solar Energy*, 127:175 – 183, 2016.

[112] F.J. Toledo and J. M. Blanes. Analytical and quasi-explicit four arbitrary point method for extraction of solar cell single-diode model parameters. *Renewable Energy*, 92:346 – 356, 2016.

[113] V. J. Chin, Z. Salam, and K. Ishaque. Cell modelling and model parameters estimation techniques for photovoltaic simulator application: A review. *Applied Energy*, 154:500 – 519, 2015.

[114] Rubitherm. Rubitherm RT-35 Phase Change Material Datasheet, 2018.

[115] *Ultralow Power Energy Harvester PMUs with MPPT and Charge Management.* Analog Devices, Sep 2016.

[116] *400mA Step-Up DC/DC Converter with Maximum Power Point Control and 250mV Start-Up.* Analog Devices, Mar 2019.

[117] *Ultralow Voltage Step-Up Converter and Power Manager.* Analog Devices, Mar 2019.

[118] A. Montecucco and A. R. Knox. Maximum power point tracking converter based on the open-circuit voltage method for thermoelectric generators. *IEEE Transactions on Power Electronics*, 30(2):828–839, Feb 2015.

[119] *EFM32 Gecko Family - EFM32G Data Sheet.* Silicon Labs, Jul 2017.

[120] *Low-Power Long Range LoRa Technology Transceiver Module.* Microchip, Apr 2017.

[121] Leonardo K.K. Maia, Lukas Drünert, Fabio La Mantia, and Edwin Zondervan. Expanding the lifetime of li-ion batteries through optimization of charging profiles. *Journal of Cleaner Production*, 225:928 – 938, 2019.

[122] Q. Wan, Y. Teh, Y. Gao, and P. K. T. Mok. Analysis and design of a thermoelectric energy harvesting system with reconfigurable array of thermoelectric generators for iot applications. *IEEE Transactions on Circuits and Systems I: Regular Papers*, 64(9):2346–2358, Sep. 2017.

[123] J. Siecker, K. Kusakana, and B.P. Numbi. A review of solar photovoltaic systems cooling technologies. *Renewable and Sustainable Energy Reviews*, 79:192 – 203, 2017.

[124] T.S. Ge, R.Z. Wang, Z.Y. Xu, Q.W. Pan, S. Du, X.M. Chen, T. Ma, X.N. Wu, X.L. Sun, and J.F. Chen. Solar heating and cooling: Present and future development. *Renewable Energy*, 126:1126 – 1140, 2018.